Geodesic Models with Convexity Shape Prior

Da Chen, Jean-Marie Mirebeau, Minglei Shu, Xuecheng Tai, Laurent D. Cohen

Geodesic Models with Convexity Shape Prior

Da Chen, Jean-Marie Mirebeau, Minglei Shu, Xuecheng Tai and Laurent D. Cohen, *Fellow, IEEE*

Abstract—The minimal geodesic models based on the Eikonal equations are capable of finding suitable solutions in various image segmentation scenarios. Existing geodesic-based segmentation approaches usually exploit image features in conjunction with geometric regularization terms, such as Euclidean curve length or curvature-penalized length, for computing geodesic curves. In this paper, we take into account a more complicated problem: finding curvature-penalized geodesic curves which are imposed a convexity shape prior. We establish new geodesic models relying on the strategy of orientation-lifting, by which a planar curve can be mapped to an high-dimensional orientation-dependent space. The convexity shape prior serves as a constraint for the construction of local geodesic metrics encoding a particular curvature constraint. Then the geodesic distances and the corresponding closed geodesic curves in the orientation-lifted space can be efficiently computed through state-of-the-art Hamiltonian fast marching method. In addition, we apply the proposed geodesic models to the active contours, leading to efficient interactive image segmentation algorithms that preserve the advantages of convexity shape prior and curvature penalization.

Index Terms—Geodesic curve, convexity shape prior, curvature penalization, Eikonal equation, fast marching, image segmentation.

1 Introduction

Image segmentation is a fundamental and challenging problem that is posed in the fields of image analysis, computer vision and medical imaging. Segmentation models based on the energy minimization frameworks are capable of coping with a great amount of complicated segmentation tasks. As important advantages, these approaches can feature significant flexibility in the accommodation of various image features, and particularly in the use of efficient shape priors for image segmentation.

The underlying energy functionals considered in many energy minimization-based segmentation models are commonly made up of an image appearance model such as the region-based homogeneity measure, and a geometry regularization term such as the curve length. Such a first-order regularizer has proven its efficiency and is commonly used in either active contour models [1]–[3] or graph-based models [4], [5]. A significant variant of the length-based regularization term can be derived by taking into account the curvature penalization [6]–[8], which usually favors smooth segmentation contours. However, applying only geometry regularities as shape priors is sometimes insufficient to search for favorable segmentation results, especially when handling images with complicated gray level distribution or weakly visible edges. In contrast, the strategy of incorporating shape-driven priors into the objective energies is able to yield more strong and efficient constraints for segmentation, thus can reduce the segmentation ambiguity. These shape priors are often carried out via a statistical model about the target shapes or contours [3], [9]–[12]. The implementation of the statistical shape priors is capable of encouraging satisfactory segmentations, even in the absence of reliable image edge saliency features and region-based appearance descriptors for the separation of disjoint and distinct object regions.

Recently, the constraints from the convexity shape and star convexity were introduced as flexible shape priors. Basically, existing image segmentation approaches in conjunction with these shape priors can be loosely categorized as either discrete or continuous types. In the discrete setting, the convexity prior [15], the star convexity prior [16], or geodesic star convexity [17] are characterized as a regularization term to construct the discrete energy functionals together with image data-driven terms. The energy minimization can be addressed by the graph cut algorithm [4]. In [18], [19], the convexity prior was incorporated into graph-based segmentation framework to solve multi-region segmentation tasks. The hedgehog-like shape prior [20] generalizes the geodesic star convexity constraint [19] to enlarge the applicable scope of the original case. Isack *et al.* [21] proposed a flexible k-convexity prior-based segmentation model which allows overlaps between different regions. However, these graph-based approaches with convexity constraint did not consider the curvature regularization.

In the continuous setting, the convexity shape prior is usually exploited as a constraint in the active contour models [22]–[25]. Among them, the curvature property is taken as a crucial feature to characterize the convexity shape prior during the curve evolution. Specifically, in [22], [24], the authors revealed the relationship between the convexity property of a region and the signed distance map associated to its boundary. They proved that a region is convex if the Laplacian of its signed distance map, which approximates the curvature of its iso-contours, has a constant sign within this region. In this approach, the convexity shape prior is used to build the search space for target regions. Shi and Li [23] introduced an alternative level set-based active contour model, in which the curvature values of the iso-contours of the level set function are leveraged to establish a convex variant of the curve evolution flow. An important shortcoming for these models is that only the sign of the curvature is utilized for segmentation, while its magnitude is ignored. Bae *et al.* [25] introduced a variant of Euler-Mumford elastica model, where the convexity constraint is implicitly taken as the regularizer of an energy, measured using the absolute curvature. Unfortunately, finding convex contours by this

- *Da Chen and Minglei Shu are are with Qilu University of Technology (Shandong Academy of Sciences), Shandong Artificial Intelligence Institute, Jinan, China. (e-mail: dachen.cn@hotmail.com)*
- *Jean-Marie Mirebeau is with Laboratoire de mathématiques d'Orsay, CNRS, Université Paris-Sud, Université Paris-Saclay, 91405 ORSAY, France. (e-mail: jean-marie.mirebeau@math.u-psud.fr)*
- *Xue-Cheng Tai Department of Mathematics, Hong Kong Baptist University, Hong Kong. (e-mail: xuechengtai@hkbu.edu.hk)*
- *Laurent D. Cohen is with University Paris Dauphine, PSL Research University, CNRS, UMR 7534, CEREMADE, 75016 Paris, France. (e-mail: cohen@ceremade.dauphine.fr)*

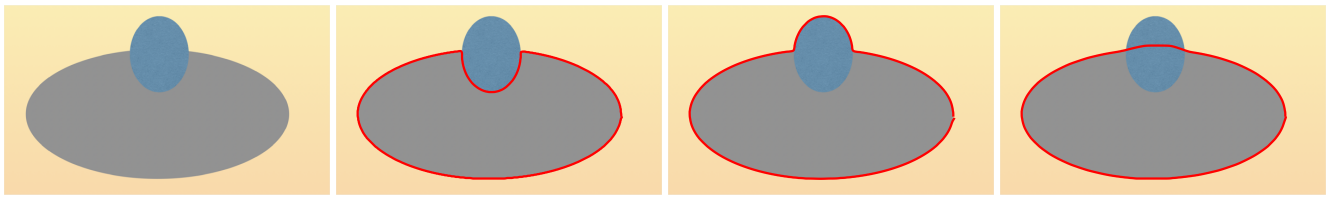

(a) (b) (c) (d)

Fig. 1. A comparison example for geodesic curves from different models. **a** A synthetic image. **c** to **d**: Results from the region-based model [13], the Euler-Mumford elastica model [14] and the proposed elastica model with convexity shape prior.

model heavily relies on the minimization of the energy, leading to a demanding requirement on the numerical scheme.

1.1 Geodesic Models

The snakes model [26] is referred to as one of the earliest variational models of leveraging continuous curves to extract image boundary features. However, the sensitivity to local minima of the snakes energy functional and the difficulty in finding suitable numerical solutions prevent this model from practical applications. In order to overcome these shortcomings, Cohen and Kimmel [27] proposed an elegant minimal path model, or geodesic model, to globally minimize a weighted curve length in an Eikonal equation framework. This original geodesic model has inspired a great variety of relevant approaches, due to its significant advantages in both global optimality and efficient numerical solvers. Among them, many geodesic models have contributed to develop various local geodesic metrics [28], [29] to extend geodesic curves to accommodate various scenarios. For instances, the curvature-penalized geodesic models introduced in [14], [30], [31] took into account an idea of orientation-lifting to address the computation problem of geodesic curves with curvature penalization. Using a suitable relaxation scheme, the geodesic distances involving curvature penalization can be efficiently estimated through the Hamiltonian fast marching method [31], [32].

In the context of image segmentation, the basic objective for geodesic-based methods is to find simple closed curves as the descriptor for boundaries of interest. Specifically, image gradients are taken as crucial features for computing geodesic curves, as considered in [33]–[35]. Moreover, Chen *et al.* [13] introduced a region-based Randers geodesic model for computing closed geodesic curves which can encode regional homogeneity features, thus build the connection between the eikonal equation-based geodesic models and the region-based active contours. In [36], the authors exploited the curvature-penalized geodesic curves for image segmentation, in which the region-based homogeneity features were implicitly encoded in the geodesic metrics.

Despite great advances, only the geometric priors (e.g. the Euclidean curve length or curvature-based length) are utilized in existing minimal geodesic approaches. In order to overcome this drawback, we introduce new geodesic models to integrate the curvature regularization, the region-based homogeneity and the convexity shape prior for computing geodesic curves, which to our best knowledge is original. Finally, in Fig. 1, we show a comparison example for geodesic curves respectively derived from two state-of-the-art geodesic models and from the proposed geodesic model with convexity shape prior. In this experiment, we aim to extract a convex ellipse shape. One can see that only the proposed geodesic model can find suitable segmentation contour, illustrating the effectiveness and necessity of imposing convexity shape prior in computing geodesic paths.

1.2 Contributions and Paper Outline

The convexity shape prior of a simple closed curve is defined by the sign of its curvature. Using this definition, we propose new geodesic models, featuring convexity shape prior, under the Eikonal equation framework. Basically, the proposed model involves the establishment of geodesic metrics and the construction of search space for admissible geodesic curves. In summary, the contributions are threefold:

– *Geodesic metrics encoding curvature restriction*. We introduce three new geodesic metrics, such that the curvature of the physical projections of the orientation-lifted geodesic curves associated to the proposed metrics have a constant sign. In addition, we also discuss the Hamiltonians of the proposed geodesic metrics, for which the discrete approximations, in terms of scalar nonnegative weights and offsets with integer components, are leveraged for finding the numerical solutions to the Eikonal equations.

– *Construction of search space for geodesic curves*. We define a search space to minimize the weighted curve length that is measured using the proposed geodesic metrics. This search space is in essence a set of admissible orientation-lifted curves, whose physical projections are supposed to be simple and closed. In particular, we work with the tool of total curvature to ensure the simplicity requirement of the search space.

– *Applications in active contours*. We investigate the applications of the proposed geodesic models in active contours and interactive image segmentation. As a consequence, the image segmentation procedure can blend the benefits from convexity shape prior, curvature regularization and image features.

The structure of this paper is organized as follows. Section 2 gives the background on the curvature-penalized geodesic models and their discretization schemes. The new geodesic models which are imposed the convexity shape prior are presented in Sections 3 and 4. The numerical implementation is presented in Section 5. In Section 6, we show how to exploit the proposed geodesic models to the active contours and image segmentation. The experimental results and the conclusion are respectively presented in Sections 7 and 8.

2 Curvature Penalized Minimal Paths

Notations. Let $\mathbb{M} := \Omega \times \mathbb{S}^1$ be an orientation-lifted space, where $\Omega \subset \mathbb{R}^2$ is a bounded domain, and $\mathbb{S}^1 := \mathbb{R}/2\pi\mathbb{Z}$ can be identified with $[0, 2\pi[$ equipped with a periodic boundary condition. A point $\mathbf{x} = (x, \theta)$ is a pair comprised of a *physical* position $x \in \Omega$ and an angular coordinate $\theta \in \mathbb{S}^1$. The tangent space to $\mathbb{M}$

is represented by $\mathbb{E} := \mathbb{R}^2 \times \mathbb{R}$, at any base point $\mathbf{x}$, and its elements are denoted $\dot{\mathbf{x}} = (\dot{x}, \dot{\theta})$. In addition, we denote by $a_+ := \max\{0, a\}$ the positive part of a real number $a \in \mathbb{R}$, and likewise $a_- := \max\{0, -a\}$. Finally, the conventions $0 \times \infty = 0$ and $a_+^2 := (a_+)^2$ are adopted in the remaining of this paper.

2.1 Orientation lifting for curvature representation

The proposed convexity-constrained geodesic models are obtained as variants of classical curvature penalized models [14], [30], [31]. Their common foundation is to evaluate curvature using an orientation lifting [37]. Consider a smooth curve $\gamma : [0, 1] \to \Omega$, with non-vanishing velocity[1]. Then there exists a unique function $\eta : [0, 1] \to \mathbb{S}^1$ obeying for all $\varrho \in [0, 1]$

$$\dot{\gamma}(\varrho) = \dot{\mathrm{n}}_{\eta(\varrho)} \|\dot{\gamma}(\varrho)\|, \tag{1}$$

where $\dot{\mathrm{n}}_\theta = (\cos\theta, \sin\theta)^\top$ denotes the unit vector of angle θ w.r.t. the horizontal axis, and $\dot{\gamma}$ is the first-order derivative of γ. Thus, $\eta(\varrho)$ encodes the tangent direction at $\gamma(\varrho)$. By (1), we define the orientation-lifted curve

$$\Gamma := (\gamma, \eta) : \varrho \in [0, 1] \mapsto \Gamma(\varrho) \in \mathbb{M}, \tag{2}$$

whose first-order derivative reads $\dot{\Gamma}(\varrho) = (\dot{\gamma}(\varrho), \dot{\eta}(\varrho)) \in \mathbb{E}$. Conversely, we refer to γ as the *physical projection*, and η as the *angular component*, of the orientation lifted curve Γ. The curvature $\kappa : [0, 1] \to \mathbb{R}$ of the planar curve γ is obtained as

$$\kappa(\varrho) = \dot{\eta}(\varrho) / \|\dot{\gamma}(\varrho)\|. \tag{3}$$

As a consequence, the curvature κ is represented through the ratio of two first-order derivatives.

2.2 Curvature Penalized Geodesic Models

In this paper, we consider three curvature-penalized minimal path models: the Reeds-Sheep forward (RSF) model [30], the Euler-Mumford (EM) elastica model [14] and the Dubins car model [31]. The energy functionals defining these models involve a scalar-valued curvature penalty function $\mathcal{C} : \mathbb{R} \to]0, \infty]$, described in Section 3. For a smooth curve $\gamma : [0, 1] \to \Omega$, with tangent direction η and curvature κ, see (1) and (3), the energy reads

$$\int_0^1 \psi(\gamma(\varrho), \eta(\varrho))\, \mathcal{C}(\beta\kappa(\varrho)) \|\dot{\gamma}(\varrho)\| d\varrho, \tag{4}$$

where $\psi : \mathbb{M} \to \mathbb{R}^+$ is a user-defined cost function, derived in this paper from the image data, see Section 6. The parameter $\beta \in \mathbb{R}^+$ has the dimension of a radius of curvature, and modulates the strength of the curvature penalty.

The curvature-penalized length (4) involves second-order derivatives of the curve γ, implicitly through $\mathcal{C}(\beta\kappa)$, and is thus not directly amenable to global optimization via the Eikonal equation framework. Using the orientation lifting (2) one can however express curvature as a ratio of first order derivatives (3), which motivates the following equivalent definition of energy

$$\mathcal{L}(\Gamma) := \int_0^1 \psi(\Gamma(\varrho))\, \mathcal{F}(\Gamma(\varrho), \dot{\Gamma}(\varrho))\, d\varrho, \tag{5}$$

where $\mathcal{F} : \mathbb{M} \times \mathbb{E} \to [0, \infty]$ is an orientation-lifted Finsler metric defined for any point $\mathbf{x} = (x, \theta) \in \mathbb{M}$ and any vector $\dot{\mathbf{x}} = (\dot{x}, \dot{\theta}) \in \mathbb{E}$. The geodesic metric can be expressed in terms of the curvature penalty function $\mathcal{C}$ and modulation parameter β [31]

$$\mathcal{F}(\mathbf{x}, \dot{\mathbf{x}}) = \begin{cases} \mathcal{C}(\beta\dot{\theta}/\|\dot{x}\|)\|\dot{x}\|, & \text{if } \dot{x} = \dot{\mathrm{n}}_\theta \|\dot{x}\|, \\ \infty, & \text{otherwise,} \end{cases} \tag{6}$$

if $\dot{x} \neq 0$. (The lower semi-continuous limit is used if $\dot{x} = 0$.)

The equivalence between the functionals (4) and (5) follows from the expression (3) of the curvature κ. Let $\mathrm{Lip}([0, 1], \mathbb{M})$ be the collection of all the orientation-lifted curves $\Gamma : [0, 1] \to \mathbb{M}$ with Lipchitz continuity. In order to compute the geodesic curve from a source point $\mathbf{p} \in \mathbb{M}$ to a target point $\mathbf{x} \in \mathbb{M}$, we first define a geodesic distance map $\mathcal{U}_\mathbf{p} : \mathbb{M} \to [0, \infty)$, also known as the minimal action map, as follows

$$\mathcal{U}_\mathbf{p}(\mathbf{x}) = \inf_{\Gamma \in \mathrm{Lip}([0,1],\mathbb{M})} \Big\{ \mathcal{L}(\Gamma);\, \Gamma(0) = \mathbf{p}, \Gamma(1) = \mathbf{x} \Big\}. \tag{7}$$

As in [31], [38], this distance map is the unique viscosity solution to a generalized Eikonal equation, or a static Hamiltonian-Jacobi equation, based on the Hamiltonian $\mathcal{H}$ of the metric $\mathcal{F}$:

$$\mathcal{H}_\mathbf{x}(d\mathcal{U}_\mathbf{p}(\mathbf{x})) = \frac{1}{2}\psi(\mathbf{x})^2, \quad \forall \mathbf{x} \in \mathbb{M} \backslash \{\mathbf{p}\}, \tag{8}$$

with $\mathcal{U}_\mathbf{p}(\mathbf{p}) = 0$, and with outflow boundary condition on $\partial\mathbb{M}$, where $d\mathcal{U}_\mathbf{p}$ stands for the differential of the geodesic distance map $\mathcal{U}_\mathbf{p}$. The Hamiltonian $\mathcal{H}$ is defined from the metric $\mathcal{F}$ by Legendre-Fenchel duality, as follows

$$\mathcal{H}_\mathbf{x}(\hat{\mathbf{x}}) := \sup_{\dot{\mathbf{x}} \in \mathbb{E}} \left\{ \langle \hat{\mathbf{x}}, \dot{\mathbf{x}} \rangle - \frac{1}{2}\mathcal{F}(\mathbf{x}, \dot{\mathbf{x}})^2 \right\} \tag{9}$$

for any point $\mathbf{x} = (x, \theta) \in \mathbb{M}$ and any co-tangent vector $\hat{\mathbf{x}} = (\hat{x}, \hat{\theta}) \in \mathbb{R}^2 \times \mathbb{R}$. Let us emphasize that the curvature penalty $\mathcal{C}$, the metric $\mathcal{F}$, and the Hamiltonian $\mathcal{H}$ have simple and explicit expressions for the models of interest, presented Section 3.

Once the distance map $\mathcal{U}_\mathbf{p}$ is known, a geodesic curve $\mathcal{G}$ from the source point $\mathbf{p}$ to an arbitrary target point $\mathbf{x} \in \mathbb{M}$ can be backtracked by solving a gradient descent-like ODE backwards in time, see [32] for a discussion of suitable numerical methods. Specifically, denoting by $T = \mathcal{U}_\mathbf{p}(\mathbf{x})$ the arrival time, one sets $\mathcal{G}(T) = \mathbf{x}$, and

$$\mathcal{G}'(\varrho) = \mathbf{V}(\mathcal{G}(\varrho)), \ \forall \varrho \in]0, T], \tag{10}$$

where geodesic flow $\mathbf{V}$ is defined from the minimal action map $\mathcal{U}_\mathbf{p}$ as follows

$$\mathbf{V}(\mathbf{x}) = d\mathcal{H}_\mathbf{x}(d\mathcal{U}_\mathbf{p}(\mathbf{x})). \tag{11}$$

In the remaining of this paper, we remove the dependency on the points $\mathbf{p}$ of the geodesic distance map $\mathcal{U}_\mathbf{p}$.

2.3 Discretization of the eikonal equation

We describe in this section the construction of a finite difference scheme approximating the generalized eikonal PDE (8), and the geodesic flow (11). These numerical methods eventually allow to compute paths globally minimizing the curvature penalized energy (4), as described Section 2.2. Our approach follows the Hamiltonian fast marching (HFM) framework [31], [32], [39].

The HFM method takes its name from a specific representation or approximation of Hamiltonian (9) involved in the eikonal PDE (8). For the models considered in this paper, this reads

$$2\mathcal{H}_\mathbf{x}(\hat{\mathbf{x}}) \approx \max_{1 \leq k \leq K} \sum_{1 \leq i \leq I} \rho_{ik}(\mathbf{x}) \langle \hat{\mathbf{x}}, \dot{\mathbf{e}}_{ik} \rangle_+^2, \tag{12}$$

1. The non-vanishing velocity assumption is implicit in the sequel.

for any point $\mathbf{x} \in \mathbb{M}$ and co-tangent vector $\hat{\mathbf{x}}$. The choice of the integers I, K, of the *non-negative* weights $\rho_{ik}(\mathbf{x}) \geq 0$, and of the offsets with *integer coordinates* $\dot{\mathbf{e}}_{ik} \in \mathbb{Z}^3$, constitutes the main originality of the HFM method [31], [32] and is discussed in detail below and in Section 3. The offsets often depend on the base point, $\dot{\mathbf{e}}_{ik} = \dot{\mathbf{e}}_{ik}(\mathbf{x})$, like the weights $\rho_{ik} = \rho_{ik}(\mathbf{x})$, but this is omitted in (12) and similar formulas for readability.

2.3.1 The finite difference scheme

The HFM method expects the domain $\mathbb{M} = \Omega \times \mathbb{S}^1$ to be discretized on a Cartesian grid

$$\mathbb{M}_h := (\Omega \cap h\mathbb{Z}^2) \times (h\mathbb{Z} \backslash 2\pi\mathbb{Z}), \tag{13}$$

where $h = 2\pi/N_\theta$ is the grid scale with N_θ being the number of discrete orientations.

Let $\mathcal{U} : \mathbb{M} \to \mathbb{R}$ be a smooth function, let $\mathbf{x} \in \mathbb{M}_h$ and let $\dot{\mathbf{e}} \in \mathbb{Z}^3$. Then one has the first order approximation

$$\langle d\mathcal{U}(\mathbf{x}), \dot{\mathbf{e}} \rangle_+^2 = \left(\frac{\mathcal{U}(\mathbf{x}) - \mathcal{U}(\mathbf{x} - h\dot{\mathbf{e}})}{h} \right)_+^2 + \mathcal{O}(h), \tag{14}$$

which only involves values of $\mathcal{U}$ at the grid points $\mathbf{x}$ and $\mathbf{x} - h\dot{\mathbf{e}}$, and is thus suitable for defining a finite difference scheme on $\mathbb{M}_h$. If $\mathbf{x} - h\dot{\mathbf{e}}$ falls outside $\mathbb{M}_h$, or if the segment $[\mathbf{x}, \mathbf{x} - h\dot{\mathbf{e}}]$ intersects an obstacle introduced in the domain as in Section 4.1 below, then we set $\mathcal{U}(\mathbf{x} - h\dot{\mathbf{e}}) = \infty$ in (14). This convention implements outflow boundary conditions.

Inserting (14) in (12) we obtain a finite differences approximation of $\mathcal{H}_{\mathbf{x}}(d\mathcal{U}(\mathbf{x}))$, with first order $\mathcal{O}(h)$ error w.r.t. the grid scale. This yields the following discretization of the eikonal equation (8): find $u : \mathbb{M}_h \to \mathbb{R}$ such that

$$\max_{1 \leq k \leq K} \sum_{1 \leq i \leq I} \rho_{ik}(\mathbf{x}) \big(u(\mathbf{x}) - u(\mathbf{x} - h\dot{\mathbf{e}}_{ik})\big)_+^2 = h^2 \psi(\mathbf{x})^2 \tag{15}$$

for all $\mathbf{x} \in \mathbb{M}_h \setminus \{\mathbf{p}\}$, with $u(\mathbf{p}) = 0$. The specific form of this numerical scheme allows to solve it very efficiently, see Section 5. The stencil of the scheme is defined as

$$\mathcal{S}(\mathbf{x}) := \{\mathbf{y}_{ik} := \mathbf{x} - h\dot{\mathbf{e}}_{ik}; 1 \leq k \leq K, 1 \leq i \leq I\}. \tag{16}$$

2.3.2 Approximation of a directional first order derivative

For the purposes of this paper, we recall one result of the HFM framework [31, Proposition 1.1], which allows in Section 3 to approximate the Hamiltonians of the models considered in this paper in the desired form (12). Specifically, given a vector $\dot{\mathbf{v}} \in \mathbb{E} \cong \mathbb{R}^3$ and a relaxation parameter $\varepsilon > 0$, one has for all co-vectors $\hat{\mathbf{x}}$:

$$\langle \hat{\mathbf{x}}, \dot{\mathbf{v}} \rangle_+^2 = \sum_{1 \leq j \leq J} \rho_j^\varepsilon(\dot{\mathbf{v}}) \langle \hat{\mathbf{x}}, \dot{\mathbf{e}}_j \rangle_+^2 + \|\hat{\mathbf{x}}\|^2 \mathcal{O}(\varepsilon^2), \tag{17}$$

where $J = 6$, the weight $\rho_j^\varepsilon(\dot{\mathbf{v}}) \geq 0$ is non-negative, and the offset $\dot{\mathbf{e}}_j = \dot{\mathbf{e}}_j^\varepsilon(\dot{\mathbf{v}}) \in \mathbb{Z}^3$ has integer components, for all $1 \leq j \leq J$, consistently with (12). An analogous result holds in two dimensions: given $\dot{v} \in \mathbb{R}^2$, $\varepsilon > 0$, one has for all $\hat{x} \in \mathbb{R}^2$

$$\langle \hat{x}, \dot{v} \rangle_+^2 = \sum_{1 \leq j \leq J'} \rho_j^\varepsilon(\dot{v}) \langle \hat{x}, \dot{e}_j \rangle_+^2 + \|\hat{x}\|^2 \mathcal{O}(\varepsilon^2), \tag{18}$$

with $J' = 3$ terms, and where $\rho_j^\varepsilon(\dot{v}) \geq 0$ and $\dot{e}_j = \dot{e}_j^\varepsilon(\dot{v}) \in \mathbb{Z}^2$ for all $1 \leq j \leq J'$.

2.3.3 The geodesic flow vector field $\mathbf{V}$

By differentiating Eq. (12), we obtain

$$d\mathcal{H}_{\mathbf{x}}(\hat{\mathbf{x}}) \approx \sum_{1 \leq i \leq I} \rho_{ik_*}(\mathbf{x}) \langle \hat{\mathbf{x}}, \dot{\mathbf{e}}_{ik_*} \rangle_+ \dot{\mathbf{e}}_{ik_*}, \tag{19}$$

where $1 \leq k_* \leq K$ is the index for which the maximum (12, right) is attained, by the envelope theorem. Inserting the finite differences (14) we can approximate the geodesic flow vector (11)

$$\mathbf{V}(\mathbf{x}) \approx h^{-1} \sum_{1 \leq i \leq I} \rho_{ik_*}(\mathbf{x}) \big(u(\mathbf{x}) - u(\mathbf{x} - \dot{\mathbf{e}}_{ik_*})\big)_+ \dot{\mathbf{e}}_{ik_*}, \tag{20}$$

where $u : \mathbb{M}_h \to \mathbb{R}$ denotes the numerical scheme solution (15).

3 Convexity-Constrained Geodesic Models

We introduce three new geodesic models featuring both a convexity shape prior and a penalization of curvature. More precisely, these models impose a constraint on the *sign* of the curvature, as motivated by the following definition.

Definition 1 (**Simple Closed Convex Curves**). *A simple closed planar curve γ, smooth and parametrized in counter-clockwise order, is said convex iff its curvature κ in Eq. (3) is non-negative.*

In the remaining of this section, we thus design curvature penalty functions $\mathfrak{C}$, which partly coincide with the penalty $\mathcal{C}$ of the RSF, Dubins and EM elastica models, but also enforce the non-negativity of the curvature. We then derive the corresponding geodesic metrics $\mathfrak{F}$, Hamiltonians $\mathfrak{H}$ and their discretizations in the HFM framework (12). In the text, the convexity constrained objects $\mathfrak{C}$, $\mathfrak{F}$, and $\mathfrak{H}$ are distinguished from their classical counterparts $\mathcal{C}$, $\mathcal{F}$, and $\mathcal{H}$ by the choice of font. Further discussion of the search space for geodesic curves, ensuring that the physical projection is simple and closed, is postponed to Section 4.

A curvature penalty $\mathfrak{C} : \mathbb{R} \to]0, \infty]$, enforcing convexity by imposing a non-negative curvature, should obey by design

$$\mathfrak{C}(\beta\kappa) = \infty \text{ if } \beta\kappa < 0. \tag{21}$$

The corresponding geodesic metric $\mathfrak{F} : \mathbb{M} \times \mathbb{E} \to [0, \infty]$, defined by (6), thus satisfies

$$\mathfrak{F}(\mathbf{x}, \dot{\mathbf{x}}) = \infty, \text{ if } \dot{\theta} < 0 \text{ or } \dot{x} \neq \dot{\mathrm{n}}_\theta \|\dot{x}\|. \tag{22}$$

for any point $\mathbf{x} = (x, \theta) \in \mathbb{M}$ and any vector $\dot{\mathbf{x}} = (\dot{x}, \dot{\theta}) \in \mathbb{E}$. The associated energy $\mathfrak{L}$ of a smooth curve $\Gamma : [0, 1] \to \mathbb{M}$ is

$$\mathfrak{L}(\Gamma) := \int_0^1 \psi(\Gamma(\varrho))\, \mathfrak{F}(\Gamma(\varrho), \dot{\Gamma}(\varrho)) d\varrho. \tag{23}$$

In view of the properties of the metric (22), any curve $\Gamma = (\gamma, \eta)$ with finite energy must obey the orientation-lifting relation (1), and have a non-decreasing angular component $\dot{\eta} \geq 0$. Finally, we infer from (9) and (22) that the Hamiltonian $\mathfrak{H}$ of a convexity-constrained model obeys

$$\mathfrak{H}((\pm\dot{\mathrm{n}}_\theta^\perp, 0)) = \mathfrak{H}((-\dot{\mathrm{n}}_\theta, 0)) = \mathfrak{H}((\mathbf{0}, -1)) = 0, \tag{24}$$

where $\dot{\mathrm{n}}_\theta^\perp$ denotes the rotation of $\dot{\mathrm{n}}_\theta$ by $\pi/2$.

Notation: In the rest of this section, we fix a base point $\mathbf{x} = (x, \theta) \in \mathbb{M}$, a vector $\dot{\mathbf{x}} = (\dot{x}, \dot{\theta}) \in \mathbb{E}$, and a co-vector $\hat{\mathbf{x}} = (\hat{x}, \hat{\theta})$.

3.1 Convex-constrained Reeds-Sheep Forward Model

For the *classical* Reeds-Sheep forward model, the curvature penalty function is defined as

$$\mathcal{C}^{\mathrm{RS}}(\beta\kappa) = \sqrt{1+(\beta\kappa)^2}. \tag{25}$$

The RSF geodesic metric $\mathcal{F}^{\mathrm{RS}}$ is obtained by incorporating $\mathcal{C}^{\mathrm{RS}}$ in the general expression (6), and thus reads

$$\mathcal{F}^{\mathrm{RS}}(\mathbf{x},\dot{\mathbf{x}}) = \sqrt{\|\dot{x}\|^2+(\beta\dot{\theta})^2} \quad \text{if } \dot{x} = \dot{\mathrm{n}}_\theta\|\dot{x}\|, \tag{26}$$

and $\mathcal{F}(\mathbf{x},\dot{\mathbf{x}}) = \infty$ otherwise. The Hamiltonian $\mathcal{H}^{\mathrm{RS}}$, obtained by specializing (9) to the RSF metric $\mathcal{F}^{\mathrm{RS}}$, admits the following closed form expression [31]

$$2\mathcal{H}^{\mathrm{RS}}_{\mathbf{x}}(\hat{\mathbf{x}}) = \langle \hat{x}, \dot{\mathrm{n}}_\theta\rangle_+^2 + (\hat{\theta}/\beta)^2. \tag{27}$$

In this paper, we consider a *convexity-constrained* RSF model defined, in view of (21), by the curvature penalty function

$$\mathfrak{C}^{\mathrm{RS}}(\beta\kappa) = \sqrt{1+(\beta\kappa)^2} \quad \text{if } \beta\kappa \geq 0, \tag{28}$$

and $\mathfrak{C}(\beta\kappa) = \infty$ otherwise. The corresponding convexity-constrained RSF metric reads, by (6)

$$\mathfrak{F}^{\mathrm{RS}}(\mathbf{x},\dot{\mathbf{x}}) = \sqrt{\|\dot{x}\|^2+(\beta\dot{\theta})^2} \quad \text{if } \dot{\theta}\geq 0 \text{ and } \dot{x} = \dot{\mathrm{n}}_\theta\|\dot{x}\|,$$

and $\mathfrak{F}^{\mathrm{RS}}(\mathbf{x},\dot{\mathbf{x}}) = \infty$ otherwise.

Proposition 1. *The Hamiltonian of the convexity-constrained RSF metric $\mathfrak{F}^{\mathrm{RS}}$ reads*

$$2\mathfrak{H}^{\mathrm{RS}}_{\mathbf{x}}(\hat{\mathbf{x}}) = \langle \hat{x}, \dot{\mathrm{n}}_\theta\rangle_+^2 + (\hat{\theta}/\beta)_+^2, \tag{29}$$

for any point $\mathbf{x} = (x,\theta) \in \mathbb{M}$ and co-vector $\hat{\mathbf{x}} = (\hat{x},\hat{\theta}) \in \mathbb{R}^3$.

Proof. Observing that $\dot{\theta}^2 = \dot{\theta}_+^2 + \dot{\theta}_-^2$, we reformulate the convexity-constrained RSF metric $\mathfrak{F}^{\mathrm{RS}}$ as follows

$$\mathfrak{F}^{\mathrm{RS}}(\mathbf{x},\dot{\mathbf{x}})^2 = \\ \langle \dot{x}, \dot{\mathrm{n}}_\theta\rangle_+^2 + \infty\langle \dot{x}, \dot{\mathrm{n}}_\theta\rangle_-^2 + \beta^2\dot{\theta}_+^2 + \infty\dot{\theta}_-^2 + \infty\langle \dot{x}, \dot{\mathrm{n}}_\theta^\perp\rangle^2,$$

with the convention $0\times\infty = 0$. Noting that $[(\dot{\mathrm{n}}_\theta,0),(\dot{\mathrm{n}}_\theta^\perp,0),(\mathbf{0},1)]$ is an orthonormal basis of $\mathbb{E}\cong\mathbb{R}^2\times\mathbb{R}$, and by general properties of Legendre-Fenchel duality (9) for quadratic functions, we obtain the expression (29) for the Hamiltonian $\mathfrak{H}^{\mathrm{RS}}$. □

We obtain using (18) an approximate decomposition of the convexity-constrained RSF Hamiltonian $\mathfrak{H}^{\mathrm{RS}}$, with a form that fits the HFM framework, and an $\mathcal{O}(\varepsilon^2)$ error,

$$2\mathfrak{H}^{\mathrm{RS}}_{\mathbf{x}}(\hat{\mathbf{x}}) \approx \sum_{1\leq j\leq J'} \rho_j^\varepsilon(\dot{\mathrm{n}}_\theta)\langle \hat{x}, \dot{e}_j\rangle_+^2 + (\hat{\theta}/\beta)_+^2.$$

Recall that $J'=3$, that $\rho_j^\varepsilon(\dot{\mathrm{n}}_\theta)\geq 0$ is a non-negative weight, and that $\dot{e}_j = \dot{e}_j^\varepsilon(\dot{\mathrm{n}}_\theta) \in \mathbb{Z}^2$ is a two dimensional offset with integer components, for all $1\leq j\leq J'$. For comparison, the original RSF Hamiltonian (27) admits a similar decomposition, used in [31], except for the last term which reads $(\hat{\theta}/\beta)^2$.

Using finite differences (14) we discretize the operator $\mathfrak{H}^{\mathrm{RS}}_{\mathbf{x}}(d\mathcal{U}(\mathbf{x}))$ of the eikonal equation (8), with consistency error $\mathcal{O}(h+\varepsilon^2)$. The scheme involves a stencil $\mathcal{S} := \mathcal{S}^{\mathrm{RS}}$ consisting of $I = J'+1 = 4$ neighbor points of $\mathbf{x}$ on the grid $\mathbb{M}_h$. Namely

$$\mathcal{S}^{\mathrm{RS}}(\mathbf{x}) := \{\mathbf{y}_i = \mathbf{x} - h\dot{\mathbf{e}}_i;\ 1\leq i\leq I\}, \tag{30}$$

where $\dot{\mathbf{e}}_i \in \mathbb{Z}^3$ is defined as $\dot{\mathbf{e}}_i = (\dot{e}_i, 0)$ for $1\leq i\leq I-1$, and $\dot{\mathbf{e}}_i = (\mathbf{0},1)$ for $i=I$.

3.2 Convex-constrained Dubins Car Model

In the *classical* Dubins model, the curvature penalty function $\mathcal{C} := \mathcal{C}^{\mathrm{D}}$ is obtained by thresholding the curvature κ, so that

$$\mathcal{C}^{\mathrm{D}}(\beta\kappa) = 1 \quad \text{if } |\beta\kappa|\leq 1, \tag{31}$$

and $\mathcal{C}^{\mathrm{D}}(\beta\kappa) = \infty$ otherwise. The Dubins geodesic metric $\mathcal{F}^{\mathrm{D}}$ is obtained by incorporating $\mathcal{C}^{\mathrm{D}}$ in the general expression (6), and thus reads

$$\mathcal{F}^{\mathrm{D}}(\mathbf{x},\dot{\mathbf{x}}) = \|\dot{x}\|, \quad \text{if } \dot{x} = \|\dot{x}\|\dot{\mathrm{n}}_\theta \text{ and } |\beta\dot{\theta}|\leq\|\dot{x}\|, \tag{32}$$

and $\mathcal{F}^{\mathrm{D}}(\mathbf{x},\dot{\mathbf{x}}) = \infty$ otherwise. The Hamiltonian $\mathcal{H}^{\mathrm{D}}$ of the Dubins metric $\mathcal{F}^{\mathrm{D}}$, defined by (9), admits the following closed form expression [31]

$$2\mathcal{H}^{\mathrm{D}}_{\mathbf{x}}(\hat{\mathbf{x}}) = \max\left\{\langle \hat{\mathbf{x}}, \dot{\mathbf{q}}^{\mathrm{D}}_+\rangle_+^2,\ \langle \hat{\mathbf{x}}, \dot{\mathbf{q}}^{\mathrm{D}}_-\rangle_+^2\right\}, \tag{33}$$

where $\dot{\mathbf{q}}^{\mathrm{D}}_+ := (\dot{\mathrm{n}}_\theta, 1/\beta)^\top$ and $\dot{\mathbf{q}}^{\mathrm{D}}_- := (\dot{\mathrm{n}}_\theta, -1/\beta)^\top$. The two vectors $\dot{\mathbf{q}}^{\mathrm{D}}_+, \dot{\mathbf{q}}^{\mathrm{D}}_- \in \mathbb{E}$ should be regarded as extremal controls, corresponding to a vehicle moving in circles of radius β, respectively in a counter-clockwise and a clockwise manner.

In this paper, we consider a *convexity-constrained* Dubins model defined, in view of (21), by the curvature penalty function

$$\mathfrak{C}^{\mathrm{D}}(\beta\kappa) = 1 \quad \text{if } 0\leq\beta\kappa\leq 1, \tag{34}$$

and $\mathfrak{C}^{\mathrm{D}}(\beta\kappa) = \infty$ otherwise. The corresponding convexity-constrained Dubins metric reads, by (6)

$$\mathfrak{F}^{\mathrm{D}}(\mathbf{x},\dot{\mathbf{x}}) = \|\dot{x}\|, \text{ if } \dot{x} = \|\dot{x}\|\dot{\mathrm{n}}_\theta \text{ and } 0\leq\beta\dot{\theta}\leq\|\dot{x}\|, \tag{35}$$

and $\mathfrak{F}^{\mathrm{D}}(\mathbf{x},\dot{\mathbf{x}}) = \infty$, otherwise.

Proposition 2. *The convexity-constrained Dubins Hamiltonian, denoted by $\mathfrak{H}^{\mathrm{D}}$, reads*

$$2\mathfrak{H}^{\mathrm{D}}_{\mathbf{x}}(\hat{\mathbf{x}}) = \max\left\{\langle \hat{\mathbf{x}}, \dot{\mathbf{q}}^{\mathrm{D}}_+\rangle_+^2, \langle \hat{x}, \dot{\mathrm{n}}_\theta\rangle_+^2\right\}. \tag{36}$$

Proof. By definition (9), and positive homogeneity of $\mathfrak{F}^{\mathrm{D}}$, one has

$$\begin{aligned}\mathfrak{H}^{\mathrm{D}}_{\mathbf{x}}(\hat{\mathbf{x}}) &= \sup_{\dot{\mathbf{x}}\in\mathbb{E}}\left\{\langle \hat{\mathbf{x}},\dot{\mathbf{x}}\rangle - \tfrac{1}{2}\mathfrak{F}^{\mathrm{D}}(\mathbf{x},\dot{\mathbf{x}})^2\right\} \\ &= \sup_{\dot{\mathbf{x}}\in\mathbb{E}}\left\{\tfrac{1}{2}\langle \hat{\mathbf{x}},\dot{\mathbf{x}}\rangle_+^2;\ \mathfrak{F}^{\mathrm{D}}(\mathbf{x},\dot{\mathbf{x}})\leq 1\right\}.\end{aligned} \tag{37}$$

The convex optimization problem (37) is posed on the set

$$\begin{aligned}\mathcal{B}^{\mathrm{D}}(\mathbf{x}) &= \{\dot{\mathbf{x}}\in\mathbb{E};\ \mathfrak{F}^{\mathrm{D}}(\mathbf{x},\dot{\mathbf{x}})\leq 1\} \\ &= \{(a\dot{\mathrm{n}}_\theta, b/\beta)\in\mathbb{E};\ 0\leq b\leq a\leq 1\}.\end{aligned}$$

The set $\mathcal{B}^{\mathrm{D}}(\mathbf{x})$, referred to as the control set of the metric $\mathfrak{F}^{\mathrm{D}}$, is a right-angled triangle, with vertices $(\mathbf{0},0)$, $\dot{\mathbf{q}}^{\mathrm{D}}_+, (\dot{\mathrm{n}}_\theta,0)\in\mathbb{E}\approx\mathbb{R}^3$. By convexity, the maximum of $\dot{\mathbf{x}}\mapsto\langle\hat{\mathbf{x}},\dot{\mathbf{x}}\rangle_+^2$ is attained at one of these vertices, as observed for a similar problem in [31]. Therefore

$$2\mathfrak{H}^{\mathrm{D}}_{\mathbf{x}}(\hat{\mathbf{x}}) = \max\{0, \langle\hat{\mathbf{x}},\dot{\mathbf{q}}^{\mathrm{D}}_+\rangle_+^2, \langle\hat{\mathbf{x}},(\dot{\mathrm{n}}_\theta,0)^\top\rangle_+^2\},$$

which concludes the proof. □

The two vectors $\dot{\mathbf{q}}^{\mathrm{D}}_+ = (\dot{\mathrm{n}}_\theta, 1/\beta)$ and $(\dot{\mathrm{n}}_\theta,0)$, involved implicitly in (36), should be regarded as extremal controls corresponding respectively to a vehicle moving in circles of radius β counter-clockwise, or moving in a straight line.

We obtain using (17) and (18) an approximate decomposition of the convexity-constrained RSF Hamiltonian $\mathfrak{H}^{\mathrm{D}}$, with a form that fits the HFM framework, and an $\mathcal{O}(\varepsilon^2)$ error,

$$2\mathfrak{H}^{\mathrm{D}}_{\mathbf{x}}(\hat{\mathbf{x}}) \approx \max\Big\{ \sum_{1\leq j\leq J} \rho^{\varepsilon}_j(\dot{\mathbf{q}}^{\mathrm{D}}_+)\langle \hat{\mathbf{x}}, \dot{\mathbf{e}}_j\rangle^2_+, \sum_{1\leq j\leq J'} \rho^{\varepsilon}_j(\dot{\mathrm{n}}_\theta)\langle \hat{x}, \dot{e}_j\rangle^2_+ \Big\}. \tag{38}$$

Recall that $J = 6$ and $J' = 3$, that $\rho^{\varepsilon}_j(\dot{\mathbf{q}}^{\mathrm{D}}_+)$ and $\rho^{\varepsilon}_j(\dot{\mathrm{n}}_\theta)$ are non-negative weights, and that $\dot{\mathbf{e}}_j = \dot{\mathbf{e}}^{\varepsilon}_j(\dot{\mathbf{q}}^{D}_+) \in \mathbb{Z}^3$ and $\dot{e}_j = \dot{e}^{\varepsilon}_j(\dot{\mathrm{n}}_\theta) \in \mathbb{Z}^2$ are offsets with integer coordinates.

Using finite differences (14) we discretize the operator $\mathfrak{H}^{\mathrm{D}}_{\mathbf{x}}(d\mathcal{U}(\mathbf{x}))$ of the eikonal equation (8), with consistency error $\mathcal{O}(h+\varepsilon^2)$. The scheme involves a stencil $\mathcal{S} := \mathcal{S}^{\mathrm{D}}$ consisting of $I = J + J' = 9$ neighbor points of $\mathbf{x}$ on the grid $\mathbb{M}_h$. Namely

$$\mathcal{S}^{\mathrm{D}}(\mathbf{x}) := \{\mathbf{y}_i = \mathbf{x} - h\dot{\mathbf{e}}_i \in \mathbb{M}_h;\ 1 \leq i \leq I\}, \tag{39}$$

where the offsets are defined by $\dot{\mathbf{e}}_i = \dot{\mathbf{e}}^{\varepsilon}_i(\dot{\mathbf{q}}^{\mathrm{D}}_+)$ for $1 \leq i \leq J$, and $\dot{\mathbf{e}}_i = (\dot{e}^{\varepsilon}_{i-J}(\dot{\mathrm{n}}_\theta), 0)$ for $J+1 \leq i \leq I$. For comparison, the original Dubins model hamiltonian $\mathcal{H}^{\mathrm{D}}$ (33) admits an approximate decomposition similar to (38) but involving the vector $\dot{\mathbf{q}}^{\mathrm{D}}_-$ instead of $\dot{\mathrm{n}}_\theta$, and a finite differences scheme based on a $J + J = 12$ points stencil [31].

3.3 Convex-constrained Euler-Mumford Elastica Model

In the *classical* EM elastica model, the curvature penalty function is defined as

$$\mathcal{C}^{\mathrm{EM}}(\beta\kappa) = 1 + (\beta\kappa)^2. \tag{40}$$

This quadratic curvature penalty is intermediate between the quasi-linear penalty of the RSF model (25), and the hard threshold of the Dubins model (31). As a result the EM elastica model assigns a high cost to path sections with large curvature, in contrast to the Dubins model which forbids them, and to the RSF model which tolerates infinite curvature (angular paths), see [31]. The elastica geodesic metric $\mathcal{F}^{\mathrm{EM}}$ reads, by (6)

$$\mathcal{F}^{\mathrm{EM}}(\mathbf{x}, \dot{\mathbf{x}}) = \|\dot{x}\| + \frac{(\beta\dot{\theta})^2}{\|\dot{x}\|} \quad \text{if } \dot{x} = \dot{\mathrm{n}}_\theta\|\dot{x}\|, \tag{41}$$

with $\mathcal{F}^{\mathrm{EM}}(\mathbf{x}, \mathbf{0}) = 0$ and and $\mathcal{F}^{\mathrm{EM}}(\mathbf{x}, \dot{\mathbf{x}}) = \infty$ otherwise. The elastica Hamiltonian $\mathcal{H}^{\mathrm{EM}}$ is derived from the metric $\mathcal{F}^{\mathrm{EM}}$ by Legendre-Fenchel duality (9), and in [31] it is shown equal to

$$2\mathcal{H}^{\mathrm{EM}}_{\mathbf{x}}(\hat{\mathbf{x}}) = \frac{1}{4}\left(\langle \hat{x}, \dot{\mathrm{n}}_\theta\rangle + \sqrt{\langle \hat{x}, \dot{\mathrm{n}}_\theta\rangle^2 + (\hat{\theta}/\beta)^2}\right)^2 \tag{42}$$

$$= \int_{-\pi/2}^{\pi/2} \big\langle \dot{\mathbf{q}}(\theta,\varphi), \hat{\mathbf{x}}\big\rangle^2_+ \cos\varphi\, d\varphi, \tag{43}$$

where we denoted

$$\dot{\mathbf{q}}(\theta,\varphi) := \tfrac{\sqrt{3}}{2}(\dot{\mathrm{n}}_\theta \cos\varphi, \beta^{-1}\sin\varphi) \in \mathbb{E} \cong \mathbb{R}^2 \times \mathbb{R}. \tag{44}$$

Somewhat curiously, the integral form (43) is more suitable for the HFM solver framework than the algebraic form (42) of the Hamiltonian. Indeed, using the Fejer quadrature rule[2] with L points we obtain with an $\mathcal{O}(1/L^2)$ error

$$2\mathcal{H}^{\mathrm{EM}}_{\mathbf{x}}(\hat{\mathbf{x}}) \approx \sum_{1\leq l\leq L} w_l \langle \hat{\mathbf{x}}, \dot{\mathbf{q}}(\theta,\varphi_l)\rangle^2_+,$$

with suitable weights $w_l \geq 0$, and with the quadrature nodes $\varphi_l := (2l - L - 1)\pi/(2L)$, for all $1 \leq l \leq L$. From this point, the approximate decomposition (17) of each of the terms $\langle \hat{\mathbf{x}}, \dot{\mathbf{q}}(\theta,\varphi_l)\rangle^2_+$, yields with (14) a finite differences scheme with an $\mathcal{O}(h + \varepsilon^2 + L^{-2})$ error and a stencil of LJ points [31]. In practice, we often use $L = 5$ which yields enough accuracy, and use the relaxation parameter $\varepsilon = 0.1$, whereas $J = 6$ by definition.

In contrast with the RSF and Dubins models, we design the *convexity-constrained* EM elastica model through a modification of Hamiltonian $\mathcal{H}^{\mathrm{EM}}$ (43), rather than of the curvature penalty function $\mathcal{C}^{\mathrm{EM}}$. More precisely, we let (notice the integral bounds)

$$2\mathfrak{H}^{\mathrm{EM}}_{\mathbf{x}}(\hat{\mathbf{x}}) := \int_0^{\pi/2} \big\langle \dot{\mathbf{q}}(\theta,\varphi), \hat{\mathbf{x}}\big\rangle^2_+ \cos\varphi\, d\varphi. \tag{45}$$

The vectors $\dot{\mathbf{q}}(\theta,\varphi)$ in (43) and (45) should be regarded as controls. When $\varphi \geq 0$ as in (45), the third component of $\dot{\mathbf{q}}(\theta,\varphi)$ is non-negative, see (44), and this control thus corresponds to a vehicle rotating clockwise. Note also that $\mathfrak{H}^{\mathrm{EM}}$ obeys (24). In the following, we compute the metric $\mathfrak{F}^{\mathrm{EM}}$ and curvature cost function $\mathfrak{C}^{\mathrm{EM}}$ corresponding to $\mathfrak{H}^{\mathrm{EM}}$, and show that they obey (22) and (21) as desired.

Before that, let us conclude the description of the numerical scheme for the convexity constrained EM elastica model. We have by (17) the approximate decomposition, with $\mathcal{O}(\varepsilon^2 + L^{-1})$ error

$$2\mathfrak{H}^{\mathrm{EM}}_{\mathbf{x}}(\hat{\mathbf{x}}) \approx \sum_{1\leq l\leq L} \tilde{w}_l \sum_{1\leq j\leq J} \rho_{jl}\langle \hat{\mathbf{x}}, \dot{\mathbf{e}}_{jl}\rangle^2_+,$$

where $\rho_{jl} = \rho^{\varepsilon}_j(\dot{\mathbf{q}}(\theta,\varphi_l))$ and $\dot{\mathbf{e}}_{jl} = \dot{\mathbf{e}}^{\varepsilon}_j(\dot{\mathbf{q}}(\theta,\varphi_l))$, and where

$$\tilde{w}_l := \begin{cases} w_l & \text{if } \varphi_l > 0, \\ w_l/2 & \text{if } \varphi_l = 0, \\ 0 & \text{else,} \end{cases} \tag{46}$$

is an adaptation of the Fejer rule for the integral (45) over the half domain $[0, \pi/2]$. Alternatively, another consistent approximation of (45), albeit with a larger consistency error, can be achieved by retaining the original Fejer weights w_l, but introducing $\tilde{\rho}_{jl} := \rho_{jl}$ if the third component of $\dot{\mathbf{e}}_{jl}$ is non-negative, and $\tilde{\rho}_{jl} := 0$ otherwise[3].

A consistent approximation of the eikonal equation operator $\mathfrak{H}(d\mathcal{U}(\mathbf{x}))$ is obtained by introducing the finite difference approximations (14), resulting in the discretized system of equations

$$\sum_{1\leq l\leq L} \tilde{w}_l \sum_{1\leq j\leq J} \rho_{jl}\left(\frac{u(\mathbf{x}) - u(\mathbf{x} - h\dot{\mathbf{e}}_{jl})}{h}\right)^2_+ = \psi(\mathbf{x})^2, \tag{47}$$

which is a special case of (15) with $K = 1$. The numerical scheme of the original EM elastica uses LJ points, but in view of (46) the stencil $\mathcal{S}^{\mathrm{EM}}$ of the convexity constrained variant only contains $I = \lceil L \rceil J$ points at most.

In the rest of this section, we obtain closed form expressions of the hamiltonian, metric, and curvature penalty, of the convexity-constrained EM elastica model. This is only motivated by a better understanding of the model, since for all practical purposes the front propagation and geodesic backtracking are implemented using (15) and (20) which only require the weights and offsets of the scheme. As a starter, we present a closed form expression of $\mathfrak{H}^{\mathrm{EM}}$ in polar coordinates.

2. The integral (43) has a cosine weight over the interval $[-\pi/2, \pi/2]$, which is equivalent to a sine weight over $[0, \pi]$, thus suitable for the Fejer rule.

3. Indeed, note that $\dot{\mathbf{e}}_{jl}$ is almost aligned with $\dot{\mathbf{q}}(\theta,\varphi_l)$, due to (17), at least when ρ_{jl} is sufficiently positive. Hence the conditions $\varphi_l \geq 0$ and $\langle \dot{\mathbf{e}}_{jl}, (\mathbf{0}, 1)\rangle \geq 0$ are closely related.

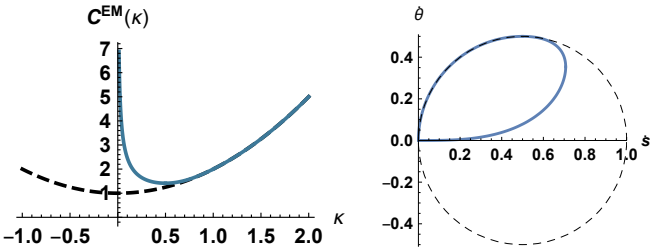

Fig. 2. **Left**: Curvature penalty $\mathcal{C}^{\mathrm{EM}}$ of the EM elastica model (dashed), and $\mathfrak{C}^{\mathrm{EM}}$ of the convexity constrained variant (thick). **Right**: Unit vectors in tangent space for the EM elastica model with and without convexity prior. Set of all $(\dot{s},\dot{\theta})$ such that $\mathfrak{F}^{\mathrm{EM}}(\mathbf{x},(\dot{s}\dot{\mathrm{n}}_\theta,\dot{\theta}))=1$ (solid line), and likewise for $\mathcal{F}^{\mathrm{EM}}$ (dashed line).

Proposition 3. *The function* $\lambda:[-\pi,\pi]\to\mathbb{R}$ *defined by*

$$\lambda(\phi):=\frac{3}{8}\int_0^{\pi/2}(\cos(\varphi-\phi))_+^2\cos\varphi\,d\varphi. \tag{48}$$

admits the explicit expression

$$8\lambda(\phi)=\begin{cases}0 & \text{if } \phi\in[-\pi,-\pi/2],\\ 2\cos\phi+2\cos\phi\sin\phi & \text{if } \phi\in[-\pi/2,0],\\ 1+\cos^2\phi+2\cos\phi\sin\phi & \text{if } \phi\in[0,\pi/2],\\ 1+\cos^2\phi+2\cos\phi & \text{if } \phi\in[\pi/2,\pi].\end{cases}$$

Also, the convexity-constrained elastica Hamiltonian $\mathfrak{H}^{\mathrm{EM}}$ *reads*

$$\mathfrak{H}^{\mathrm{EM}}_{\mathbf{x}}(\hat{\mathbf{x}})=r^2\lambda(\phi),\quad \text{when } (\langle\hat{x},\dot{\mathrm{n}}_\theta\rangle,\hat{\theta}/\beta)=r(\cos\phi,\sin\phi),$$

for some $r>0$ *and* $\phi\in[-\pi,\pi]$.

Proof. By considering the sign of $\cos(\phi-\varphi)$, we find that $\lambda(\phi)$ is the integral of the trigonometric expression $\cos(\varphi-\phi)^2\cos\varphi$ over the interval $\emptyset$, $[0,\pi/2+\phi]$, $[0,\pi/2]$, and $[\phi-\pi/2,\pi/2]$ respectively in each of the four distinguished cases. The expression of $\lambda(\phi)$ easily follows. Finally we observe that

$$\begin{aligned}\frac{2}{\sqrt{3}}\langle\dot{\mathbf{q}}(\theta,\varphi),\hat{\mathbf{x}}\rangle&=\langle\hat{x},\dot{\mathrm{n}}_\theta\rangle\cos\varphi+\frac{\hat{\theta}}{\beta}\sin\varphi\\&=r(\cos\varphi\cos\phi+\sin\varphi\sin\phi)=r\cos(\varphi-\phi),\end{aligned}$$

and the expression of $\mathfrak{H}^{\mathrm{EM}}$ follows from (45). □

The metric $\mathfrak{F}^{\mathrm{EM}}$ can be expressed in terms of the Hamiltonian $\mathfrak{H}^{\mathrm{EM}}$ using Legendre-Fenchel duality, inverting the relation (9):

$$\frac{1}{2}\mathfrak{F}^{\mathrm{EM}}(\mathbf{x},\dot{\mathbf{x}})^2=\sup_{\hat{\mathbf{x}}}\left\{\langle\hat{\mathbf{x}},\dot{\mathbf{x}}\rangle-\mathfrak{H}^{\mathrm{EM}}_{\mathbf{x}}(\hat{\mathbf{x}})\right\}. \tag{49}$$

Denoting $\dot{s}:=\|\dot{x}\|$ and $\dot{\nu}:=\beta\dot{\theta}$, the metric $\mathfrak{F}^{\mathrm{EM}}$ reads for any non-zero vector $\dot{\mathbf{x}}=(\dot{x},\dot{\theta})\in\mathbb{E}$

$$\mathfrak{F}^{\mathrm{EM}}(\mathbf{x},\dot{\mathbf{x}})^2= \tag{50}$$
$$\begin{cases}+\infty, & \text{if } \dot{\theta}<0 \text{ or } \dot{x}\neq\dot{\mathrm{n}}_\theta\|\dot{x}\|,\\ \frac{8}{27\dot{\nu}}(9\dot{s}\dot{\nu}^2+\dot{s}^3+(\dot{s}^2-3\dot{\nu}^2)^{\frac{3}{2}}) & \text{if } 0<\dot{\nu}\le\dot{s}/2,\\ 4(\dot{s}^2-2\dot{s}\dot{\nu}+2\dot{\nu}^2), & \text{if } 0\le\dot{s}/2\le\dot{\nu}\le\dot{s},\\ (\dot{s}+\dot{\nu}^2/\dot{s})^2, & \text{if } 0\le\dot{s}\le\dot{\nu}.\end{cases}$$

Sketch of proof of (50). The announced expression of $\mathfrak{F}^{\mathrm{EM}}$ was obtained with the help of the formal computing program Mathematica®. We only show here how it can be checked formally, once it is known. Define the Lagrangian

$$\mathcal{L}_{\mathbf{x}}(\dot{\mathbf{x}}):=\frac{1}{2}\mathfrak{F}^{\mathrm{EM}}(\mathbf{x},\dot{\mathbf{x}})^2,$$

as defined from (50), and denote the Hamiltonian $\mathfrak{H}_{\mathbf{x}}(\hat{\mathbf{x}}):=\mathfrak{H}^{\mathrm{EM}}_{\mathbf{x}}(\hat{\mathbf{x}})$. Our objective is to establish (49), in other words that $\mathcal{L}_{\mathbf{x}}$ is the Legendre-Fenchel dual of $\mathfrak{H}_{\mathbf{x}}$. This relation is characterized[4] by the identity

$$\mathcal{L}_{\mathbf{x}}(\nabla\mathfrak{H}_{\mathbf{x}}(\hat{\mathbf{x}}))=\mathfrak{H}(\hat{\mathbf{x}}) \tag{51}$$

for any co-vector $\hat{\mathbf{x}}\in\mathbb{E}^*$. Recalling that $\mathfrak{H}_{\mathbf{x}}(\hat{\mathbf{x}})=r^2\lambda(\phi)$ from Proposition 3, and differentiating in these polar-like coordinates, we obtain

$$\nabla\mathfrak{H}_{\mathbf{x}}(\hat{\mathbf{x}})=2r\lambda(\phi)(\dot{\mathrm{n}}_\theta\cos\phi,\frac{\sin\phi}{\beta})+r\lambda'(\phi)(-\dot{\mathrm{n}}_\theta\sin\phi,\frac{\cos\phi}{\beta})$$

In the sequel we assume that $r=1$, for simplicity and w.l.o.g. by homogeneity of $\mathfrak{H}$ and $\mathcal{L}$. In view of (50), we define $\dot{s}$ and $\dot{\nu}$ by $\nabla\mathfrak{H}_{\mathbf{x}}(\hat{\mathbf{x}})=\dot{\mathbf{x}}=(\dot{x},\dot{\theta})=(\dot{s}\,\dot{\mathrm{n}}_\theta,\dot{\nu}/\beta)$, in other words

$$\begin{aligned}\dot{s}&=2\lambda(\phi)\cos\phi-\lambda'(\phi)\sin\phi,\\ \dot{\nu}&=2\lambda(\phi)\sin\phi+\lambda'(\phi)\cos\phi.\end{aligned}$$

In order to conclude the proof, we need to insert the explicit expression of λ, distinguishing cases depending on the interval containing ϕ. If $\phi\in[-\pi,\pi/2]$, then $\lambda(\phi)=\lambda'(\phi)=0$, thus $\dot{s}=\dot{\nu}=0$ and therefore both sides of (51) are zero. If $\phi\in[-\pi/2,0]$, then we obtain $8\dot{s}=2(2\cos\phi+2\cos\phi\sin\phi)\cos\phi-(-2\sin\phi-2\sin^2\phi+2\cos^2\phi)\sin\phi$, and likewise $\dot{\nu}$ is a polynomial function of $\cos\phi$ and $\sin\phi$. A long and tedious sequence of elementary trigonometric identities, which is not presented here, and which is within the grasp of symbolic computation methods, yields the inequality $0\le\dot{\nu}\le\dot{s}/2$ and the identity

$$\frac{8}{27\dot{\nu}}(9\dot{s}\dot{\nu}^2+\dot{s}^3+(\dot{s}^2-3\dot{\nu}^2)^{\frac{3}{2}})=2\cos\phi+2\cos\phi\sin\phi,$$

which is equivalent to (51) when $\phi\in[-\pi/2,0]$. (Use that $\dot{s}^2-3\dot{\nu}^2=(\cos2\phi-\sin\phi)^2/16$.) Proving (51) thus reduces, likewise when $\phi\in[0,\pi/2]$ and $\phi\in[\pi/2,\pi]$, to checking an inequality and an equality between suitable polynomials in the variables $\cos\phi$ and $\sin\phi$, which follows from elementary (yet tedious) computations. □

The curvature penalty of the convexity constrained EM model can be recovered from the metric and the relation $\mathfrak{C}^{\mathrm{EM}}(\beta\kappa)=\mathfrak{F}^{\mathrm{EM}}(\mathbf{x},(\dot{\mathrm{n}}_\theta,\kappa))$, in view of (6). This also amounts to choosing $\dot{s}=1$ and $\dot{\nu}=\beta\kappa$ in (50), and therefore

$$\mathfrak{C}^{\mathrm{EM}}(\dot{\nu})=\begin{cases}+\infty & \text{if } \nu\le0\\ \sqrt{\frac{8}{27\dot{\nu}}(9\dot{\nu}^2+1+(1-3\dot{\nu}^2)^{\frac{3}{2}})} & \text{if } 0<\dot{\nu}\le1/2\\ 2\sqrt{1-2\dot{\nu}+2\dot{\nu}^2} & \text{if } 1/2\le\dot{\nu}\le1,\\ 1+\dot{\nu}^2, & \text{if } 1\le\dot{\nu}.\end{cases}$$

The penalty $\mathfrak{C}^{\mathrm{EM}}$ is infinite when the path curvature is negative, as expected, and coincides with the original EM elastica model $\mathcal{C}^{\mathrm{EM}}$ when $1\le\dot{\nu}:=\beta\kappa$, in other words when the path curvature exceeds $1/\beta$. Note that straight line segments have finite energy for the convexity constrained Reeds-Shepp and Dubins models, since $\mathfrak{C}^{\mathrm{RS}}(0)=\mathfrak{C}^{\mathrm{D}}(0)=1$, whereas the EM variant only allows strictly convex paths, since $\mathfrak{C}^{\mathrm{EM}}(0)=\infty$. The curvature penalty function $\mathfrak{C}^{\mathrm{EM}}$, and the set of all $(\dot{s},\dot{\theta})$ such that $\mathfrak{F}^{\mathrm{EM}}(\mathbf{x},(\dot{s}\dot{\mathrm{n}}_\theta,\dot{\theta}))=1$ with $\beta=1$, are illustrated in Fig. 2.

4. And in addition $\mathcal{L}_{\mathbf{x}}(\dot{\mathbf{x}})=\infty$ when $\dot{\mathbf{x}}$ is not in the range of $\nabla\mathfrak{H}$, which is readily checked.

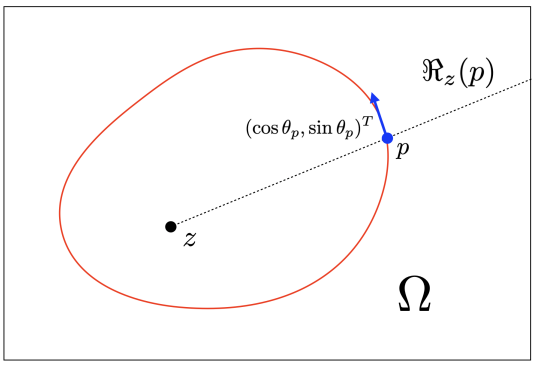

Fig. 3. The black dash line indicates the ray line $\Re_z(p)$, which originates from the physical position z (black dot) and passes through p (blue dot). The arrow stands for the direction of $(\cos\theta_p, \sin\theta_p)^\top$, respectively.

4 Extracting Simple Closed Convex Curves

We have introduced in Section 3 three metrics $\mathfrak{F}$, on the state space $\mathbb{M} = \Omega \times \mathbb{S}^1$ of positions and orientations, featuring both a convexity shape prior and a curvature regularization. In this section, we address the problem of tracking orientation-lifted geodesics $\mathcal{G} := (\mathcal{C}, \eta)$, with respect to the chosen metric $\mathfrak{F}$, whose physical projection $\mathcal{C} \in C^2([0,1], \Omega)$ on the physical space Ω is simple closed and convex. Moreover, we introduce an additional constraint ensuring that the planar curve $\mathcal{C}$ encloses a given point in Ω, so as to accommodate practical segmentation tasks.

Toward that purpose, we define a reduced domain $\tilde{\mathbb{M}}$, by removing an appropriate region which acts as a wall, and choose a specific start and endpoint $\mathbf{p}$, see Section 4.1. The work presented in this paper is a variant of the circular geodesic model [33]. It combines constraints on the physical projection $\mathcal{C}$ and the angular component η of the curve, so as to control the total curvature and eliminate curves whose physical projection has *self-intersections*.

4.1 Endpoints and Artificial Obstacles

The circular geodesic (CG) model [33] is a practical method for extracting closed planar geodesic curves within the image domain Ω. Our variant of this model requires the user to fix a planar point $z \in \Omega$, and an orientation lifted point $\mathbf{p} = (p, \theta_p) \in \mathbb{M} = \Omega \times \mathbb{S}^1$, subject to the compatibility condition $\det(p - z,\ \dot{\mathrm{n}}_{\theta_p}) > 0$.

In the context of interactive image segmentation, it is natural to place the point p on the boundary of the target region, with θ_p denoting the tangent orientation of this boundary in the trigonometric orientation. The point z is placed inside the target convex region, allowing the user to guide the image segmentation in a simple and reliable manner. A crucial ingredient of the CG model is a ray line, i.e. a half line, introduced within the domain Ω and defining a cut which locally disconnects its two sides. More precisely, the ray line $\Re_z(p)$ originating from z and passing through p is regarded as an obstacle. We also introduce a barrier at the position θ_p in the angular domain. See Fig. 3, where $\Re_z(p)$ is dotted, the angular coordinate θ_p of $\mathbf{p}$ is indicated by the arrow $(\cos\theta_p, \sin\theta_p)^\top$, and an admissible path γ is shown. The accessible domain remaining for the orientation-lifted geodesic paths is thus

$$\tilde{\mathbb{M}} := \{(x, \theta) \in \mathbb{M};\ x \notin \Re_z(p) \text{ and } \theta \neq \theta_p\}. \tag{52}$$

Our method exploits a path of minimal energy $\mathfrak{L}$, from the point $\mathbf{p}$ to itself, and within the obstacle free domain $\tilde{\mathbb{M}}$: we solve

$$\inf \Big\{ \mathfrak{L}(\Gamma); \Gamma \in C^1([0,1], \mathbb{M}), \\ \Gamma(0) = \Gamma(1) = \mathbf{p}, \Gamma(\varrho) \in \tilde{\mathbb{M}}, \forall \varrho \in]0,1[\Big\}. \tag{53}$$

We show in Section 4.2 that the physical projection of any candidate minimizer to the problem (53) is a simple closed and convex curve enclosing the point z, and we describe Section 5 a global numerical optimization procedure.

4.2 Total Curvature and Curve Simplicity

In this section, we show that the constraints of (53) ensure the simplicity of the physical projection γ of any admissible orientation-lifted curve $\Gamma = (\gamma, \eta)$.

For that purpose, let us summarize the properties obeyed by a candidate minimizer $\Gamma = (\gamma, \eta)$ to the optimization problem (53):

$$\gamma(0) = \gamma(1) = p, \qquad \eta(0) = \eta(1) = \theta_p, \tag{54}$$
$$\gamma(\varrho) \notin \Re_z(p), \qquad \eta(\varrho) \neq \theta_p, \tag{55}$$
$$\dot\gamma(\varrho) = \dot{\mathrm{n}}_{\eta(\varrho)} \|\dot\gamma(\varrho)\|, \qquad \dot\eta(\varrho) \geq 0. \tag{56}$$

The first line follows from the boundary condition $\Gamma(0) = \Gamma(1) = \mathbf{p}$. The second line holds for $\varrho \in]0,1[$ and follows from the choice (52) of the obstacle free domain $\tilde{\mathbb{M}}$. The third line holds for $\varrho \in [0,1]$, and follows from $\mathfrak{L}(\Gamma) < \infty$ (otherwise Γ is not a candidate minimizer) and from the choice of metric, see Eqs. (22) and (23).

The rest of this section will be devoted to the proof of the following proposition.

Proposition 4. *Assume that $(\gamma, \eta) \in C^1([0,1], \mathbb{M})$ obeys (54), (55), (56), and that γ' is non-vanishing over $[0,1]$. Then the curve γ is simple, closed, convex, and encloses the point z. Furthermore, the total (absolute) curvature of γ is 2π.*

Proof. We introduce a parametric function $\underline{\eta} :]0,1[\to \mathbb{R}$ such that $\underline{\eta}(\varrho) \equiv \eta(\varrho) \pmod{2\pi}$, for all $\varrho \in]0,1[$, and likewise $\underline{\theta}_p \in \mathbb{R}$ such that $\underline{\theta}_p \equiv \theta_p \pmod{2\pi}$. We may assume that $\underline{\eta}(0) = \underline{\theta}_p$, by (54, right). Observe that $\underline{\eta}(\varrho)$ is non-decreasing, by (56, right), and that $\underline{\eta}(\varrho) \notin \theta_p + 2\pi\mathbb{Z}$ for all $\varrho \in]0,1[$, by (55, right). As a result

$$\underline{\theta}_p < \underline{\eta}(\varrho) < \underline{\theta}_p + 2\pi,\ \forall \rho \in]0,1[, \tag{57}$$

and finally $\underline{\eta}(1) = \underline{\theta}_p + 2\pi$, by (54, right).

The path γ has a non-vanishing velocity, and obeys the lifting compatibility condition (56, left), hence its curvature is obtained as $\kappa = \dot\eta / \|\dot\gamma\|$, see (3). Note that the curvature κ is non-negative, by (56, right), and thus equal to the absolute curvature. The total curvature of γ (absolute or otherwise) is obtained as

$$\mathcal{K}(\gamma) = \int_0^1 \kappa(\varrho)\, \|\dot\gamma(\varrho)\|\, d\varrho = \int_0^1 \dot\eta(\varrho)\, d\varrho, \tag{58}$$

and therefore, in view of previously established properties of $\underline{\eta}$

$$\mathcal{K}(\gamma) = \int_0^1 \dot{\underline{\eta}}(\varrho)\, d\varrho = \underline{\eta}(1) - \underline{\eta}(0) = (\theta_p + 2\pi) - \theta_p = 2\pi.$$

Consider $0 \leq \varrho_1 < \varrho_2 < 1$ such that $\eta(\varrho_1) = \eta(\varrho_2)$, if they exist. Then from (57) and the monotony of η we obtain $\underline{\eta}(\varrho) = \underline{\eta}(\varrho_1)$ for all $\varrho_1 \leq \varrho \leq \varrho_2$, hence γ that is restricted to $[\varrho_1, \varrho_2]$ is a straight segment, and therefore the tangent lines at $\gamma(\varrho_1)$ and at

$\gamma(\varrho_2)$ coincide. It easily follows that there are no three[5] points of γ such that the tangents at these points are pairwise distinct and parallel, and thus that γ is the boundary of a convex set $R \subset \mathbb{R}^2$.

By construction, the boundary ∂R intersects the half line $\Re_z(p)$ at the point p and nowhere else. Recalling that $\det(p - z, \dot{\mathrm{n}}_{\theta_p}) > 0$ we see that $\Re_z(p)$ is not tangential to ∂R, and thus R contains the bounded connected component of $\Re_z(p) \setminus \{p\}$, which is the segment $[z, p[$. In other words, the curve γ encloses the point z, and the announced result follows. □

5 Numerical Solutions

Let us consider the path-length quasi-distance function $\mathcal{D}$ that is defined by

$$\mathcal{D}(\mathbf{x}, \mathbf{y}) := \inf \Big\{ \mathfrak{L}(\Gamma); \Gamma \in C^1([0,1], \tilde{\mathbb{M}}), \\ \Gamma(0) = \mathbf{x}, \Gamma(1) = \mathbf{y} \Big\},$$

for all points $\mathbf{x}, \mathbf{y}$ of the obstacle free domain $\tilde{\mathbb{M}}$, see (52). We set here the objective of computing the distance $\mathcal{D}(\mathbf{p}_0, \mathbf{p}_1)$ with

$$\mathbf{p}_0 := (p + \varepsilon \dot{\mathrm{n}}_{\theta_p}, \theta_p + \varepsilon), \quad \mathbf{p}_1 := (p - \varepsilon \dot{\mathrm{n}}_{\theta_p}, \theta_p - \varepsilon), \quad (59)$$

where $\mathbf{p} = (p, \theta_p)$ is a user defined orientation-lifted point, see Section 4.1, and $\varepsilon > 0$ is a small parameter. Letting $\varepsilon \to 0$, we recover the original problem (53) of finding a path from $\mathbf{p}$ to itself, within $\tilde{\mathbb{M}}$ and minimizing $\mathfrak{L}$. Note that the endpoints $\mathbf{p}_0, \mathbf{p}_1$ may be replaced with any small perturbations of $\mathbf{p}$ whose components lie on the similar side of the obstacle $\Re_z(p)$ in the planar domain, and of the obstacle $\{\theta_p\}$ in the angular domain. In practice, we may choose the points of the discretization grid $\mathbb{M}_h$, see (13), which are the closest to $\mathbf{p}$ and obey these geometrical constraints.

Define the geodesic distance map $\mathcal{U} : \tilde{\mathbb{M}} \to [0, \infty]$ by

$$\mathcal{U}(\mathbf{x}) := \mathcal{D}(\mathbf{p}_0, \mathbf{x}). \quad (60)$$

This function obeys the eikonal equation $\mathfrak{H}(\nabla \mathcal{U}(\mathbf{x})) = \frac{1}{2}\psi(\mathbf{x})^2$ on $\tilde{\mathbb{M}} \setminus \{\mathbf{p}_0\}$, with $\mathcal{U}(\mathbf{p}_0) = 0$ and with outflow boundary conditions on $\partial\tilde{\mathbb{M}}$. Here $\mathfrak{H}$ is the Hamiltonian corresponding to one of the convexity constrained geodesic models, see Section 3.

A numerical solution $u : \mathbb{M}_h \to \mathbb{R}$ to the discretized eikonal equation (15) is computed, using one of the solvers described in the next subsection. Once u is known, a globally optimal path from $\mathbf{p}_0$ to $\mathbf{p}_1$ can be extracted by backtracking as defined in Eq. (10), based on the expression (20) of the geodesic flow.

5.1 Solving for the Distance Map

In this section, we briefly discuss the numerical computation of the unique solution to the discretized eikonal equation (15), which is quite standard. Indeed, our main contributions lies in the design of the curvature constrained models, of the scheme coefficients and offsets, and of the artificial obstacles, see Sections 3 and 4. For simplicity, we assume w.l.o.g. that the desired path endpoints $\mathbf{p}_0, \mathbf{p}_1$ belong to the discretization grid $\mathbb{M}_h$, see (13) and (59).

For numerical purposes, an array of unknowns $u : \mathbb{M}_h \to \mathbb{R}$ is introduced, and initialized to $u(\mathbf{p}_0) = 0$ and $u = \infty$ elsewhere on $\mathbb{M}_h \setminus \{\mathbf{p}_0\}$. In the course of the numerical solver, the unknown is updated by solving locally the numerical scheme (15), at some given point $\mathbf{x} \in \mathbb{M}_h \setminus \{\mathbf{p}_0\}$. In such an update, we assign $u(\mathbf{x}) \leftarrow \mathrm{u}$, where u solves

$$\max_{1 \le k \le K} \sum_{1 \le i \le I} \rho_{ik}(\mathbf{x})(\mathrm{u} - \mathrm{u}_{ik})_+^2 = h^2 \psi(\mathbf{x})^2, \quad (61)$$

and where for all $1 \le i \le I$ and $1 \le k \le K$ one has denoting $\mathbf{y}_{ik} := \mathbf{x} - h\dot{\mathbf{e}}_{ik}$

$$\mathrm{u}_{ik} = \begin{cases} +\infty & \text{if } \mathbf{y}_{ik} \notin \mathbb{M}_h \text{ or } [\mathbf{x}, \mathbf{y}_{ik}] \not\subset \tilde{\mathbb{M}}, \\ +\infty & \text{if } \mathbf{y}_{ik} \text{ not ACCEPTED}, \\ u(\mathbf{y}_{ik}) & \text{else.} \end{cases} \quad (62)$$

The first line serves to apply outflow boundary conditions on $\partial\mathbb{M}$, and to avoid any front propagation across the obstacles introduced in $\tilde{\mathbb{M}}$, whereas the second line is specific to the fast marching numerical method, see below. Note that letting $\mathrm{u}_{ik} = \infty$ is equivalent to ignoring the contribution of the stencil point $\mathbf{y}_{ik}$, since the update equation involves the difference $(\mathrm{u} - \mathrm{u}_{ik})_+$. Once the values $(\mathrm{u}_{ik})_{1 \le i \le I}^{1 \le k \le K}$ are gathered and sorted, one can find the update value u by solving at most KI univariate polynomial equations of degree two, since (61, l.h.s.) is a piecewise quadratic function of u. A similar procedure was already used in [40].

The ordering of the updates (61) depends on the numerical solver used. On a CPU processor, the fast marching algorithm [40] is used, which is made possible by the mathematical structure[6] of the scheme as in [31], [32], [39]. This method works in a single pass over the domain (the points of $\mathbb{M}_h$ are successively ACCEPTED one by one based on a priority queue) and has complexity $\mathcal{O}(N \ln N)$ where $N = \#(\mathbb{M}_h)$ is the number of discretization points. The front propagation can be stopped as soon as the target point $\mathbf{p}_1$ is reached. If a GPU accelerator is available, on the other hand, then a variant of the massively parallel fast iterative method [41] is used (which does not involve ACCEPTED tags). The increased complexity of this approach, namely $\mathcal{O}(N^{1+1/d})$ with $d = 3$, and the stricter stopping criterion, namely global convergence of u, are more than compensated by the massive thread parallelism, resulting in a $15\times$ or better speedup in applications.

Let us mention that it is possible to track the the total curvature $\mathcal{K}$ of the minimal paths by adapting a numerical method [42], originally introduced to simultaneously estimate the weighted length and the Euclidean length of geodesic curves between $\mathbf{p}_0$ and any point $\mathbf{x}$, without backtracking these curves. By the arguments of Section 4.2, this is not necessary to ensure that the paths is simple and convex, provided the front propagation is restrained to the obstacle free domain (52) using proper intersection tests for the offsets as in (62, first line). In fact, by tracking and limiting the total curvature one eliminates the need for the obstacle $\{\theta_p\}$ in the angular domain $\mathbb{S}^1$, whose implementation can be inconvenient due to the periodic boundary condition, so this remains an option.

6 Applications to Active Contours

In this section, we show the possibility of applying the proposed geodesic models with convexity shape prior to address the active contour problems.

5. If the tangent lines at $\gamma(\varrho_1)$, $\gamma(\varrho_2)$ and $\gamma(\varrho_3)$ are parallel, then $\eta(\varrho_1) \equiv \eta(\varrho_2) \equiv \eta(\varrho_3) \pmod{\pi}$, thus by the pigeonhole principle one has e.g. $\eta(\varrho_1) \equiv \eta(\varrho_2) \pmod{2\pi}$, and then by the previous argument the tangents at $\gamma(\varrho_1)$ and $\gamma(\varrho_2)$ are identical.

6. Namely, that (61) is a non-decreasing function of $[(\mathrm{u} - \mathrm{u}_{ik})_+]_{1 \le i \le I}^{1 \le k \le K}$.

6.1 Computation of Region-based Velocity

6.1.1 Region-based Randers Geodesic Model

We start from a typical active contour energy functional comprising of a region-based homogeneity term Ξ and a regularization term Φ

$$E(\gamma) := \mu\,\Xi(\gamma) + \Phi(\gamma), \tag{63}$$

where $\mu > 0$ is a positive constant and $\gamma \in \mathrm{Lip}([0,1],\Omega)$ is a closed curve. In general, the term $\Phi(\gamma)$ can be defined as a weighted curve length w.r.t. a Riemannian metric, of the form

$$\Phi(\gamma) = \int_0^1 \|\dot\gamma(\varrho)\|_{\mathcal{M}(\gamma(\varrho))}\, d\varrho.$$

The metric tensor $\mathcal{M}$ is derived from the image gradients, in such way that $\|\dot x\|_{\mathcal{M}(x)} = \sqrt{\langle \dot x, \mathcal{M}(x)\dot x\rangle}$ is low [14] when an edge passes by the point $x \in \Omega$ with a tangent direction that approximates the unit vector $\dot x$.

The region-based term Ξ, also referred to as the image appearance model, measures the homogeneity of image features in each region. In this section, we take the region competition model [43] with the Gaussian mixture model (GMM) as an example to formulate the region-based term

$$\Xi(\gamma) = \int_{R_1} \xi_1(x)dx + \int_{R_2} \xi_2(x)dx, \tag{64}$$

where R_1 and R_2 are the regions inside and outside the closed curve γ. The scalar-valued functions $\xi_i : \Omega \to \mathbb{R}$ $(i = 1, 2)$ encode the image homogeneity features within each region R_i. We compute each ξ_i using a Gaussian mixture model, for which the probability distribution function (PDF) $P_i(z;\Theta_i)$ is taken as a weighted sum of N Gaussian PDFs. Let $f : \Omega \to \mathbb{R}^d$ be an image, where $d = 1$ (resp. $d = 3$) implies that f is a gray level (resp. color) image. Then one has

$$\xi_i(x) = -\log\big(P_i(f(x);\Theta_i)\big),\ \forall x \in \Omega, \tag{65}$$

where Θ_i are the parameters of the PDFs of the GMM.

Moreover, the piecewise constant appearance model [44] is known as an efficient variant of the GMM-based term Ξ. In this case, the function ξ_i can be computed as

$$\xi_i(x) = \int_{R_i} \|f(x) - \mathfrak{c}_i\|^2 dx, \tag{66}$$

where $\mathfrak{c}_i = (c_{i,1}, c_{i,2}, c_{i,3}) \in \mathbb{R}^d$ such that $c_{i,j}$ with $1 \le j \le d$ stands for the mean intensity of the j-th image channel within each corresponding region R_i.

In the region-based geodesic model [13], [45], image segmentation is solved by minimizing the energy E as formulated in (63). A key ingredient for the EAC model is to express, using Stokes theorem, the energy (63) as a weighted curve length, i.e. $E(\gamma) = \tilde\Phi(\gamma) + \sigma$, where σ is a scalar value independent of γ, and where

$$\tilde\Phi(\gamma) = \int_0^1 \|\dot\gamma(\varrho)\|_{\mathcal{M}(\gamma(\varrho))} + \mu\langle \varpi(\gamma(\varrho)), \dot\gamma(\varrho)\rangle d\varrho. \tag{67}$$

The vector field $\varpi : \mathbb{R}^2 \to \mathbb{R}^2$ is defined over an open bounded region $U \subset \Omega$, and is obtained as the solution of the linear PDE

$$\min \int_{\mathbb{R}^2} \|\varpi(x)\|^2 dx,\ s.t.\ \mathrm{curl}\,\varpi = (\xi_1 - \xi_2)\chi_U, \tag{68}$$

where $\chi_U : \mathbb{R}^2 \to \{0,1\}$ is the characteristic function of the subdomain U. The solution to the linear problem (68) can be obtained by convolution of the r.h.s. $(\xi_1 - \xi_2)\chi_U$ with a suitable kernel [45]. In a variant of (68), used in the experiments, the objective function is replaced with $\int_U \|\varpi(x)\|^2 dx$, so that a staggered grid finite difference method can be used over the domain U, which provides less guarantees but often yields better numerical behavior [45].

The weighted length (67) is an instance of Randers geometry, defined by a non-symmetric metric

$$\mathfrak{R}(x,\dot x) = \|\dot x\|_{\mathcal{M}(x)} + \mu\langle \varpi(x), \dot x\rangle. \tag{69}$$

It is proven in [45] that the metric $\mathfrak{R}$ is positive definite provided the region U is sufficiently small and the first order term is defined by (68). During the curve evolution, U should be understood as the search space for the evolving curves.

6.1.2 Orientation-lifted Velocity

The weighted curve length (67) can be theoretically interpreted in the framework of orientation lifting, by choosing the cost $\psi(x,\theta) = \mathfrak{R}(x, \dot{\mathrm{n}}_\theta)$. This leads to the possibility of integrating the region-based homogeneity features and curvature regularization for solving the active contour problems, using a sufficiently small U to ensure the positivity of $\psi(x,\theta)$. However, such an interpretation is not what we do in this paper. In contrast, we construct the velocity ψ as an exponential cost of the components of the metric $\mathfrak{R}$. Specifically, we consider

$$\psi(x,\theta) = \begin{cases} \exp\left(\alpha\,\tilde\psi(x,\theta)\right), & \forall x \in U, \\ \infty, & \text{otherwise}, \end{cases} \tag{70}$$

where $\alpha > 0$ is a constant and where the function $\tilde\psi$ is defined as

$$\tilde\psi(x,\theta) := \frac{\|\dot{\mathrm{n}}_\theta\|_{\mathcal{M}(x)}}{\sup\limits_{(y,\vartheta)\in\mathbb{M}} \|\dot{\mathrm{n}}_\vartheta\|_{\mathcal{M}(y)}} + \frac{\mu\langle \varpi(x), \dot{\mathrm{n}}_\theta\rangle}{\sup\limits_{y\in\Omega}\|\varpi(y)\|}. \tag{71}$$

This construction of ψ proves to be very efficient in practice, although the connection with (63) and (67) is partly lost.

6.2 Convexity-constrained Active Geodesic Paths for Interactive Image Segmentation

We apply the proposed geodesic models imposed with convexity shape prior for interactive image segmentation in conjunction with a curve evolution manner. The evolving curves are the physical projections of the orientation-lifted geodesic paths. When the evolution stabilizes, the target boundaries can be delineated by the obtained physical projection curves, generated using the proposed geodesic models with convexity shape prior. The proposed interactive segmentation algorithm can be divided into two steps: (i) establishing extra constraints for geodesic paths from user-specified annotations, and (ii) evolving the geodesic paths associated to the proposed geodesic models. In the following, we will present the details for those steps.

6.2.1 Extra Constraints for Geodesic Paths

Scribbles-based Annotations. Scribbles are very often taken as initial annotations in interactive segmentation algorithms. Here we propose a way for geodesic-based segmentation, which allows to leverage foreground and background scribbles as extra constraint. In our model, each scribble is regarded as a subregion of the image domain Ω. We can randomly sample a point x_F from each foreground scribble $F \subset \Omega$. The union $([z, x_F] \cup F) \times \mathbb{S}^1$ serves

Fig. 4. An example for initialization derived from the landmark points-based annotation. The blue and cyan dots in columns 1 to 4 denote the landmark points. Column 1: The cyan dot together with the cyan arrows indicate the source point $\mathbf{p}$. Column 2: the blue transparent region indicates the convex hull of all the landmark points with the red dot being its barycenter center. Column 3: the green lines represent the additional obstacles. Column 4: Segmentation contour indicated by the red line.

Fig. 5. An example for initialization derived from the scribbles-based annotation. The blue and red curvilinear structures in columns 1 to 4 represent the interior and exterior scribbles, respectively. Column 1: The cyan dot together with the cyan arrows indicate the source point $\mathbf{p}$. Column 2: the blue transparent region indicates the convex hull. Column 3: the green lines represent the additional obstacles. Column 4: Segmentation contour indicated by the red line.

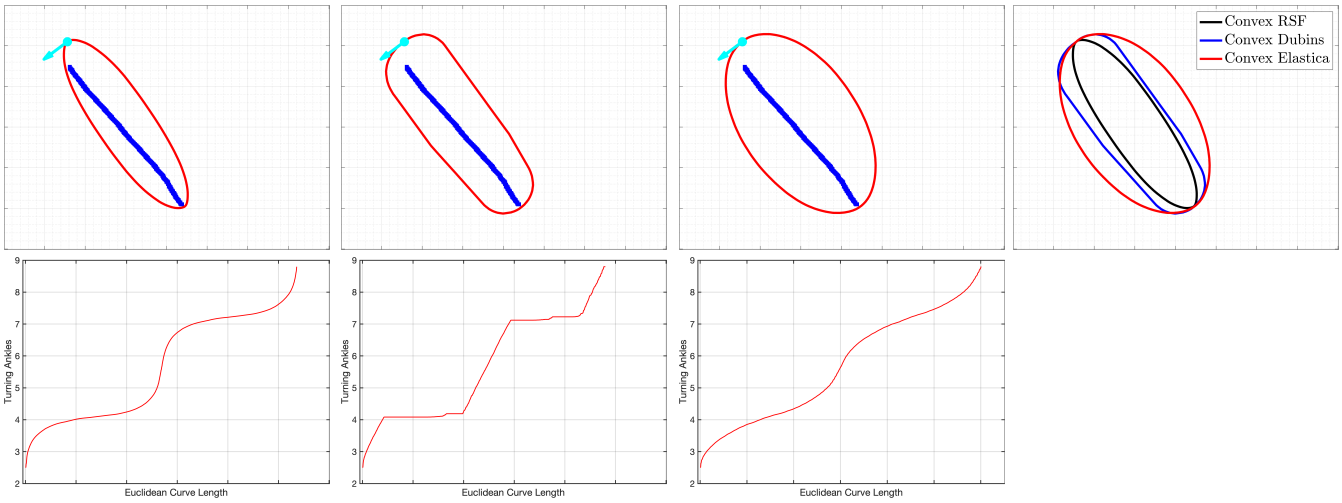

Fig. 6. **Top**: The geodesic paths (red lines) in columns 1 to 3 are respectively derived from the proposed RSF-Convexity, Dubins-Convexity and Elastica-Convexity models. The blue curvilinear structures are the foreground scribbles, and the cyan dots with arrows represent the source point. **Bottom**: The plots of the turning angles of the corresponding orientation-lifted geodesic paths.

as an obstacle such that no curve is allowed to passed through it. At the same time, one can choose a point x_B from each background scribble $B \subset \Omega$. This point can yield a segment $[x_B, q]$ where $q \in \partial\Omega$ is a point subject to $(z - x_B) \propto (x_B - q)$. Similarly to $([z, x_F] \cup F) \times \mathbb{S}^1$, the union $([x_B, q] \cup B) \times \mathbb{S}^1$ also forms an obstacle in the search space of geodesic paths.

When numerically computing geodesic distance values by the HFM method, any point $\mathbf{y}$ will be removed from the stencil $\mathcal{S}(\mathbf{x})$ if the segment $[\mathbf{x}, \mathbf{y}]$ intersects the obstacles generated by the scribbles and the point z.

Landmark points-based Annotations. In the context of interactive image segmentation, boundary-based annotations are usually carried out by a family of landmark points x_k, indexed by $1 \leq k \leq \mathfrak{K}$, such that each point x_k is placed at the target boundary. In contrast to traditional approaches [35], we *do not* impose any order to the points x_k.

Let $\Re_z(x_k)$ be a ray line or half straight line emanating from z and passing through x_k, and let q_k be the intersection point between $\Re_z(x_k)$ and the target boundary. It is easy to see that the orientation-lifted geodesic paths do not pass through the wall $[z, x_k[\times \mathbb{S}^1$ and $]x_k, q_k] \times \mathbb{S}^1$, due to the convex assumption on their physical projections. Note that for each index k, neither $[z, x_k[$ nor $]x_k, q_k]$ involves the landmark point x_k. Numerically, when computing geodesic distances by the HFM method, the walls $[z, x_k[\times \mathbb{S}^1$ and $]x_k, q_k] \times \mathbb{S}^1$ are used to refine the stencils $\mathcal{S}$. Specifically, a point $\mathbf{y} \in \mathcal{S}(\mathbf{x})$ should be excluded from $\mathcal{S}(\mathbf{x})$,

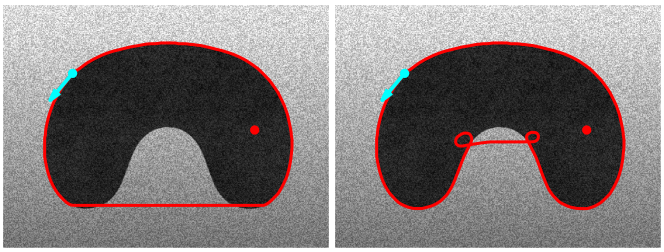

(a) (b)

Fig. 7. An example for geodesic curves with (left) or without (right) the constraint on the bound of the total curvature, respectively. The red dots indicate the physical position z and the cyan dots together with the cyan arrows represent the source point $\mathbf{p} = (p, \theta_p)$.

if the segment $[\mathbf{x}, \mathbf{y}]$ satisfies that $[\mathbf{x}, \mathbf{y}] \cap ([z, x_k[\times \mathbb{S}^1) \neq \emptyset$, or $[\mathbf{x}, \mathbf{y}] \cap (]x_k, q_k] \times \mathbb{S}^1) \neq \emptyset$. As a result, the physical projection of any closed geodesic paths $\mathcal{G}$, subject to $\mathcal{G}(0) = \mathcal{G}(1) = \mathbf{p}$, will pass through all landmark points x_k.

Automatic Detection of the point z. The point z used for defining the search space of geodesic paths can be automatically derived from the user annotations. By the convexity assumption of the target regions, it is natural to set the point z as the barycenter of the convex hull of the set $\{p,\, x_k; k = 1, \cdots, \mathfrak{K}\}$ (resp. $F \cup \{p\}$ with F being all the foreground scribbles) for the landmark points-based (resp. scribbles-based) annotation way, where p is the physical position of the source point $\mathbf{p} = (p, \theta_p)$. In this way, one can point out that the detected point z must lie at the interior of the target region.

6.2.2 *Active Geodesic Evolution Procedure*

In this section, we incorporate the proposed geodesic models with convexity shape prior into the region-based Randers geodesic model [45], such that the image segmentation can preserve the advantages of user annotations, curvature regularization and convexity shape constraint.

Using a curve evolution scheme, the goal is to generate a sequence of closed geodesic paths $\{\mathcal{G}_j\}_{j\geq 0}$, each of which lies at the space $\mathbb{M}$ and solves the problem (53) and is such that the physical projection $\mathcal{C}_j$ is a simple closed and convex planar curve, obeying $\mathcal{C}_j(\varrho) \in U_j, \forall \varrho \in [0, 1]$. In this way, the search space U_j at the j-th iteration is used to find the solution to the problem (68), in order to update the velocity ψ_j through Eq. (70). Moreover, as in the region-based geodesic model [45], we choose the search space U_j as a tubular neighbourhood of $\mathcal{C}_{j-1}$.

Recall that the initialization for the proposed geodesic models requires a point $z \in R$ with $R \subset \Omega$ being the target region, and an orientation-lifted point $\mathbf{p} = (p, \theta_p) \in \mathbb{M}$ such that $p \in \partial R$, as described in Section 4.1. In addition to these points, we take into account two types of interaction ways for building the sequence $\{\mathcal{G}_j\}_{j\geq 0}$, in order to accommodate complicated situations.

Building the initial curves. The initial curve $\mathcal{G}_0 = (\mathcal{C}_0, \eta_0)$ should obey that (i) $\mathcal{G}_0(0) = \mathbf{p}$, and (ii) the physical projection $\mathcal{C}_0$ is simple closed and convex. In order to simplify the initialization process of the proposed segmentation method, we construct the initial curve $\mathcal{G}_0$ as a closed minimal path by solving the problem (53), subject to the user-provided annotations discussed above.

The image gradients-based features are independent to the evolving geodesic curves $\mathcal{G}_j$. As a consequence, such an initial curve $\mathcal{G}_0$ can be produced using the edge-based features only. We denote by ψ_{edge} such an edge-based velocity that reads

$$\psi_{\text{edge}}(x, \theta) = \exp\left(\frac{\|\dot{\mathfrak{n}}\|_{\mathcal{M}(x)}}{\sup\limits_{(y,\vartheta)\in\mathbb{M}} \|\dot{\mathbf{n}}_\vartheta\|_{\mathcal{M}(y)}}\right), \forall x \in \Omega, \quad (72)$$

which is independent to the tubular neighbourhood U_j for any $j \geq 0$.

7 Experimental Results

In this section, the numerical experiments are mainly dedicated to illustrate the advantages of exploiting the convexity shape prior and the curvature penalty for image segmentation. We firstly study the properties of the proposed three geodesic models. Following that, we focus on the qualitative and quantitative comparisons against the graph-based segmentation model with convexity shape constraint (Graph-Convexity) [15], and the geodesic paths-based segmentation approaches involving the region-based Randers geodesic (RandersGeo) model [45] and the instances of curvature-penalized geodesic models [14], [30]. In addition, when tracking closed geodesic paths, we exploit the same strategy with the proposed models except that the total curvature constraint on geodesic curves is removed to the RandersGeo model and the curvature-penalized geodesic models, as discussed in Section 4.

7.1 Properties of the Proposed Geodesic Models

We first illustrate in Fig. 7 the effect of the wall in the angular domain, which amounts to a constraint on the total curvature, and which guarantees the simplicity of the target physical projection curves, see Proposition 4. In this figure, the cyan dots and the respective cyan arrows indicate the source point $\mathbf{p} = (p, \theta_p)$. The red lines are the physical projections of the extracted geodesic paths. Figs. 7a and 7b respectively illustrate the results of the proposed Elastica-Convexity model with and without the total curvature constraint. In Fig. 7a, one can observe that the closed curve indicated by a red line is simple and convex. In contrast, in Fig. 7b, the absence of the constraint on the bound of the total curvature (58) leads to the self-crossing phenomenon. Moreover, the lack of the total curvature constraint also yields a non-convex closed curve, proving its importance and necessity in the proposed models.

In Fig. 6, we present a numerical experiment to illustrate the qualitative differences between the proposed geodesic models with convexity shape prior, by choosing a constant velocity $\psi \equiv 1$ and the parameter $\beta = 4$, see Eq. (23), for each tested geodesic model. The red lines shown in the top row of columns 1 to 3 represent the physical projections of the geodesic paths, which are respectively generated through the RSF-Convexity, Dubins-Convexity and Elastica-Convexity models. These paths are obtained by performing the HFM algorithm just once, as discussed in Section. 6.2. In the bottom row, we plot the turning angles (i.e. the angular coordinate η) of the orientation-lifted geodesic paths $\Gamma = (\gamma, \eta)$, each of which is parameterized by the Euclidean curve length of γ. The physical projection curves corresponding to the RSF-Convexity and Elastica-Convexity models appear to be smooth. Specifically, the physical projection curve associated to the RSF-Convexity model allows the presence of high curvature values, which also can be seen from the plot of the turning angles (as shown in the bottom row of column 1). In the top row of

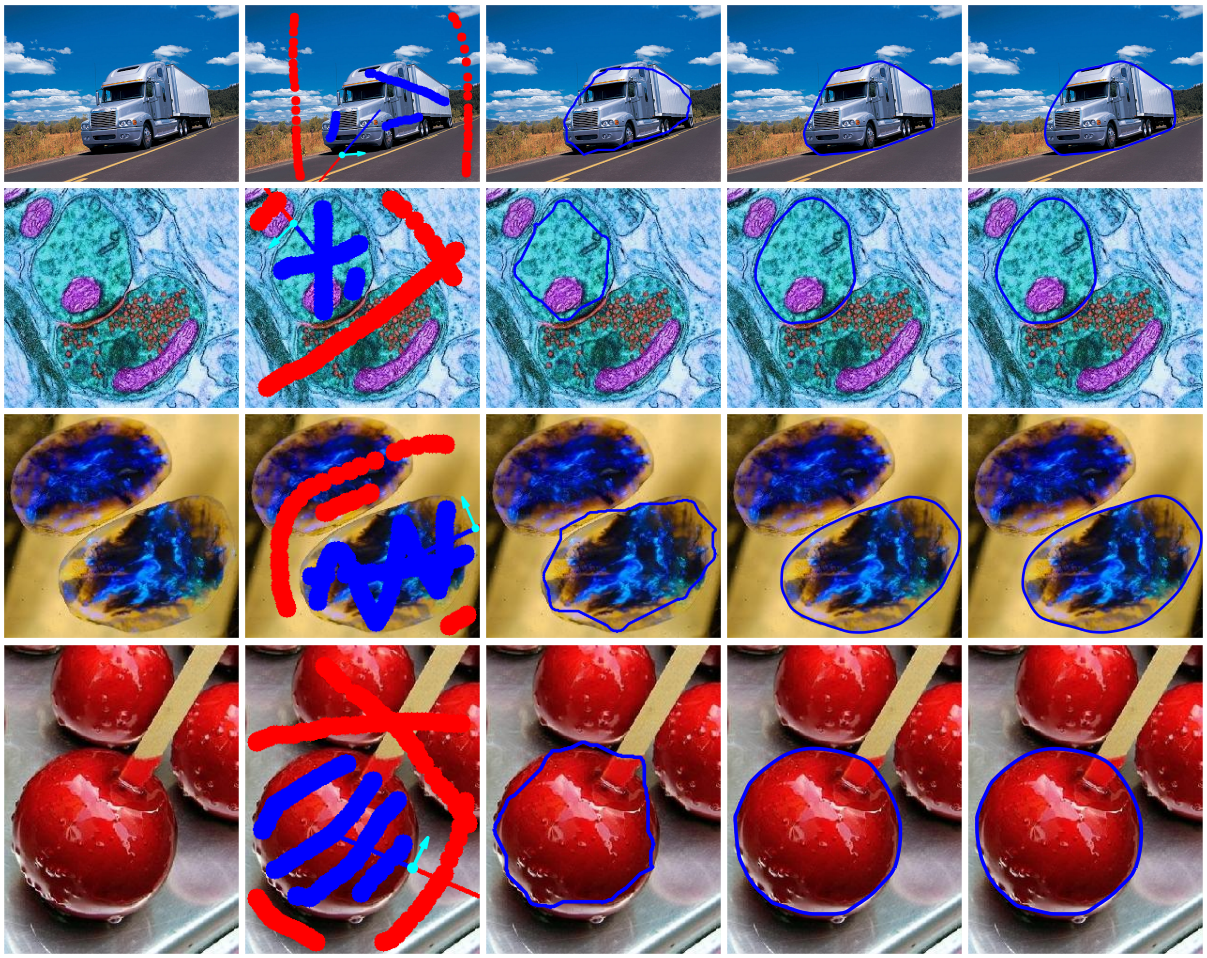

Fig. 8. Qualitative comparison results with the Graph-Convexity model. Column 1: Original images. Column 2: Initializations. The blue and red curvilinear structures denote the scribbles inside and outside the target regions. The cyan dots and the respective arrows indicate the source points. Columns 3 to 5: Segmentation results from different models.

column 2, the physical projection curve associated to the Dubins-Convexity model can be approximately divided into straight segments and parts of circles, which is also discussed in [32]. Such an observation can be verified by the plot of turning angles, the graph of which is the concatenation of straight segments of different slopes. Moreover, we notice that the plots of the turning angles for all the proposed models indicate non-decreasing curvature values, consistently with Definition 1. Finally, the qualitative differences between the proposed geodesic models are quite similar to those between the original curvature-penalized geodesic models [32], due to their relevance.

Notice that in both the original Dubins model and its convexity-constrained variant, the parameter β defines a hard constraint on the the curvature of the geodesic curves. This lack of flexibility means that the parameter β must be finely tuned, otherwise the desired contour may not be admissible, which prevents the practical applications of the Dubins model in image analysis. Accordingly, in the remaining of this section, we focus on the qualitative and quantitative evaluation of the performance of the RSF-Convexity and Elastica-Convexity models.

7.2 Qualitative Comparisons

In order to set up the proposed geodesic models with convexity shape prior, we need to give the values of the related parameters. Specifically, we choose the parameters $\alpha \in \{3, 4\}$ and $\mu \in \{0.1, 1\}$ for the computation of the velocity defined in Eq. (70), and fix the parameter $\beta = 1$ for the relative importance of the curvature term. The relaxation parameter $\epsilon = 0.1$ is used for the numerical schemes of the HFM method. In the following experiments, the point z is generated automatically using the procedure presented in Section 6.2. In addition, unless otherwise specified, we apply the identical velocity ψ and identical values of parameters β, ξ to the instances of the classical curvature-penalized models and the proposed geodesic models with convexity shape constraint.

In Fig. 8, we illustrate the qualitative comparison results with the Graph-Convexity model on the images chosen from the Convexity dataset [15]. The original images and the initial annotations are respectively shown in columns 1 and 2, where the red and blue dots respectively represent the point z and the physical position p of the source point $\mathbf{p} = (p, \theta_p)$. The cyan arrow is positively collinear to $(\cos\theta_p, \sin\theta_p)^\top$. For the Graph-Convexity model, we leverage the seeded annotations provided by the authors [15] as the foreground and background scribbles. For

Fig. 9. Qualitative comparison results with state-of-the-art geodesic models. Columns 1 and 2 show the original images as well as the corresponding annotations. The blue structures in column 2 denote the scribbles inside the target regions. The cyan dots and the respective arrows indicate the source points. Columns 3 to 5: Image segmentation results from different models.

TABLE 1
Quantitative comparison of different models by the average and standard deviation values of Jaccard scores on 5 images shown in Fig. 10.

IMAGES	Row 1		Row 2		Row 3		Row 4		Row 5	
JS / Models	Ave.	Std.	Ave.	Std.	Ave.	Std.	Ave.	Std.	Ave.	Std.
Graph-Convexity	59.16%	0.04	69.80%	0.05	87.23%	0.01	92.38%	0.01	96.04%	0.02
RandersGeo	86.31%	0.01	88.35%	0.02	85.34%	0.01	77.66%	0.14	89.42%	0.00
Classical Elastica	72.03%	0.07	92.04%	0.01	84.66%	0.03	78.21%	0.15	89.91%	0.01
Elastica-Convexity	**88.62%**	0.02	**95.58%**	0.00	**90.30%**	0.01	**99.63%**	0.00	**99.49%**	0.00

fair comparison, we add the segment $[z, p]$ (resp. the segment $[p, q]$ such that $q \in \partial\Omega$ subject to $(p - z) \propto (q - p)$) to the foreground scribbles (resp. to the background scribbles). In column 3 of Fig. 8, we can see that the segmentation regions from [15] indeed appear to be approximately convex, but fail to accurately recover the objective regions. In contrast, the proposed RSF-Convexity and Elastica-Convexity models are capable of yielding smooth and accurate segmentation contours, as shown in columns 4 and 5. Moreover, the segmentation results from both of the proposed geodesic models are quite close to each other, despite their different regularities on the curvature.

Fig. 9 presents a qualitative comparison of the proposed Elastica-Convexity geodesic model and state-of-the-art geodesic models including the RandersGeo and original elastica models on images sampled from the dataset [15]. The annotations shown in column 2 are exploited to initialize these models. In this experiment, there is no background scribble provided for interactive segmentation. It is known that the RandersGeo model heavily depends on the region-based homogeneity features and the edge-based features, as described in Section 6.1. Accordingly, when these features are unreliable for defining the target boundaries, low quality of segmentation results may be yielded by this model, due to the absence of the convexity shape prior. This is also the case for the classical elastica model in conjunction with edge-based features, though the use of the curvature regularity may slightly increase the smoothness of the segmentation contours, as depicted in column 4. While in column 5, the smooth and tight segmentation contours are obtained from the proposed Elastica-Convexity model, which can suitably delineate the target boundaries, thanks to the integration of convexity shape prior, curvature regularization and image features. Note that in this experiment the classical elastica geodesic model was applied with hybrid image features which include both the image gradients features and the region-based homogeneity features.

Fig. 10 depicts the comparison results obtained from the Graph-Convexity model, the RandersGeo model, the classical elastica geodesic model with hybrid image features, and the proposed Elastica-Convexity model. Among the results shown in

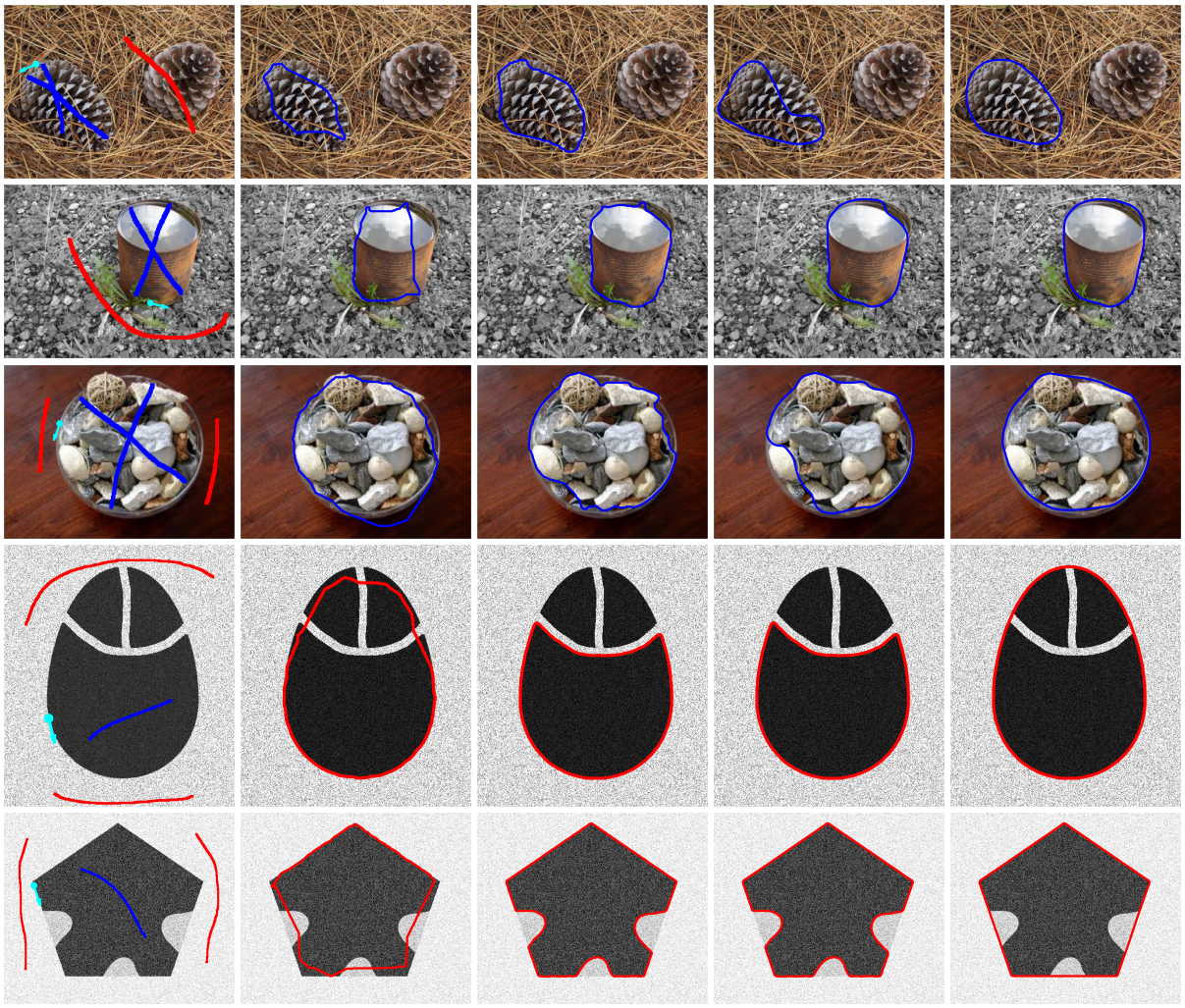

Fig. 10. Qualitative comparison results with state-of-the-art geodesic models. Columns 1 show the original images with the initial annotations. The blue and red curvilinear structures denote the scribbles inside and outside the target regions. The cyan dots and the corresponding arrows indicate the source points. Columns 2 to 5: Image segmentation results from different models.

rows 1 to 3, we observe that the proposed Elastica-Convexity model can produce accurate segmentation contours. While for the other compared models, some segments of the desired boundaries are missed. The images in rows 1 to 3 are sampled from the Weizmann dataset [46]. In rows 4 and 5 of Fig. 10, we illustrate the segmentation results on synthetic images blurred by gaps and noise. The goal is to search for the boundaries of the ellipse and polygon shapes as shown in rows 4 and 5, respectively. In these synthetic images, the Graph-Convexity model can produce convex shapes as segmentations. However, these shapes fail to completely recover the true objective regions, due to sensitivity to the locations of the scribbles. Finally, we found that the RandersGeo and classical elastica models produce non-convex contours, thus missing some parts of the desired boundaries, due to the influence of the gaps. Note that in Figs 8 to 10, we utilize the GMM-based image appearance model for computing the region-based homogeneity features.

7.3 Quantitative Comparisons

In this section, we present the quantitative comparison results of different models. These experiments are conducted using different initial annotations. In each test, we apply the Jaccard scores for the measurement of the accuracy of the segmentation results. Let SR and GR respectively denote the segmented region generated from the tested models and the ground truth region. The Jaccard score, denoted by $\mathrm{JS} \in [0, 1]$, is an estimation of the quality that the region SR recovers the ground truth region GR, which reads

$$\mathrm{JS}(\mathrm{SR}, \mathrm{GR}) := \frac{|\,\mathrm{SR} \cap \mathrm{GR}\,|}{|\,\mathrm{SR} \cup \mathrm{GR}\,|}, \tag{73}$$

where $|\,\mathrm{SR}\,|$ is the area of the region SR.

Table 1 presents the quantitative comparison results of the proposed Elastica-Convexity model with the Graph-Convexity model, the RandersGeo model, and the classical elastica models. This experiment is conducted on the images shown in Fig. 10, by varying the source point $\mathbf{p}$ along the ground truth boundary. For each test image, we select 10 (physical) points from its ground truth boundary and manually assign to each point a tangent. We further assume that these sampled points distribute evenly along the boundary. By running the compared models 10 times per test image upon these source points, the average and standard deviation values of Jaccard scores are obtained. From Table 1, we

TABLE 2
Quantitative comparison of different models (applied with Scribbles- and Landmark points-based annotations) by the average and standard deviation values of Jaccard scores on the Convexity dataset.

Annotations	Scribbles		Five Landmark Points	
JS / Models	Ave.	Std.	Ave.	Std.
Graph-Convexity	85.10%	0.08	71.40%	0.15
RandersGeo	86.71%	0.10	86.95%	0.07
Classical Elastica	88.44%	0.08	90.38%	0.04
Elastica-Convexity	**90.66%**	0.06	**92.17%**	0.03

TABLE 3
Quantitative comparison of different models (applied with landmark points-based annotations) by the average and standard deviation values of Jaccard scores on the Convexity dataset.

Num. Points	Three Points		Four Points	
JS / Models	Ave.	Std.	Ave.	Std.
RandersGeo	79.94%	0.12	82.56%	0.10
Classical Elastica	81.70%	0.11	86.72%	0.07
Classical Elastica (Edge)	75.86%	0.13	83.20%	0.08
Elastica-Convexity	**84.05%**	0.10	**88.82%**	0.05

can see that the proposed model achieve the best performance in terms of the average values of the scores. Particularly, the Graph-Convexity and the proposed Elastica-Convexity models outperform the RandersGeo and classical elastica models in the synthetic images, because the latter are attracted by non-convex apparent gaps along the boundary.

The quantitative performance of the proposed Elastica-Convexity model as shown in Table 1 is indeed promising, but insufficient to fully access the ability of the proposed models in finding suitable results under various initial annotations. For this purpose, we perform the quantitative comparison of the proposed Elastica-Convexity model to the Graph-Convexity, RandersGeo and classical elastica geodesic models on the Convexity dataset [15], under different initial annotations. The comparison results are presented in Table 2. In the second column of this table, the scribbles are obtained from the Convexity dataset, augmented with the external scribbles generated from the source point $\mathbf{p}$. In this experiment, the geodesic path-based approaches *do not use* the exterior scribbles from the Convexity dataset for the segmentation process, in contrast with the Graph-Convexity method. For each test image, we sample 5 source points $\mathbf{p}$ which are evenly distributed at the ground truth contour. Each source point together with the scribbles will produce a JS value, and we take the average of the obtained 5 JS values as the *mean accuracy score* for this test image. The Ave. and Std. values in this table represent the average and standard deviation of the mean accuracy scores of all the images in the Convexity dataset. In the third column of Table 2, the tested models are configured in terms of landmark points. Similar to the scribbles-based case, we randomly choose 5 sets of landmark points for each image, where each set is comprised of 5 points. In addition, we take one point as the physical position p of the source point, and manually specify the corresponding angle θ_p. One can see that in both annotations, the proposed Elastica-Convexity model obtains the highest mean accuracy scores among all the tested models.

In Table 3, we show the quantitative comparison with different geodesic models over the Convexity dataset, using the landmark points-based annotation for initialization. In this experiment, we perform the segmentation process using 3 and 4 points, respectively shown in the second and third columns, to configure the tested models. In a test, the used 3 (or 4) points are chosen as a subset of the sampled points used in the experiment of Table 2. Note that the geodesic paths from the model named *Classical Elastica (Edge)*, relying only on the image gradients, are the initial curves for the Classical Elastica model. In this table, we also observe that the proposed Elastica-Convexity model outperforms the other compared geodesic models, even when using fewer landmark points.

7.4 Discussion on Computation Times

The computation complexity in our model is dominated by the estimation of the GMM-based velocity and the running of the HFM algorithm in the course of the curve evolution. We focus on the analysis on the HFM algorithm, since the velocity estimation is embarrassingly parallel and could thus easily be accelerated using GPU programming. The computation complexity $\mathcal{O}(IK\,N \ln N)$ of the HFM method depends on the number N of discretization points of the grid, and the number IK of points in the stencil (16). Practical run times also modestly depend on the test case specific parameters, such as the such as the relaxation parameter $\varepsilon > 0$ used for the curvature penalized models [31], the profile of the cost function and walls, and more importantly the use of a narrow band which constrains the front propagation to a small subregion. The experiments were conducted on an Intel Core i9 3.6GHz architecture with 96GB RAM, using a C++ implementation. We take the image shown in Fig. 1 as an example to report the execution time, where the size of the grid is $346 \times 599 \times 60$. The HFM method associated to the Elastica-Convexity model requires around 38 seconds for tracking the geodesic path as indicated by the red line in Fig. 1d. No narrow band was considered in this test, which relied on a gradients-based velocity. A GPU implementation of the eikonal solver [47] led to a strong acceleration, and to running times compatible with user interaction. In the same example Fig. 1d, computation time is reduced to 2.5 seconds on a laptop equipped with an Nvidia 2060 Max-Q GPU.

8 Conclusion

In this paper, we show the possibility of imposing the convexity shape prior to existing curvature-penalized geodesic models, known as the Reeds-Sheep forward, Dubins car and Euler-Mumford elastica models. The expected planar convex contours are obtained as the physical projections of the geodesic curves from the proposed geodesic models. We addressed two crucial issues in order to generate such geodesic curves, including (i) the construction of new geodesic metrics which admit particular constraint derived from the convexity shape prior, and (ii) the design of the set collecting all admissible orientation-lifted curves whose physical projections satisfy the closedness and simplicity restriction. Furthermore, we introduced two ways to apply the proposed geodesic models for interactive image segmentation, such that the user intervention, involving either landmark points or scribbles, can be efficiently incorporated in the computation of geodesic curves. Experimental results on both synthetic and real images illustrated the advantages of the proposed models, when

comparing to the graph-based models with convexity shape prior and state-of-the-art geodesic models.

The future work will be dedicated to the development of more feasible image segmentation strategies based on the proposed geodesic models with convexity shape prior, in conjunction with more complicated image appearance models.

ACKNOWLEDGEMENT

The authors would like to thank the editor and all the reviewers for their valuable times to review this manuscript.

REFERENCES

[1] T. F. Chan, B. Y. Sandberg, and L. A. Vese, "Active contours without edges for vector-valued images," *J. Vis. Commun. Image Represent.*, vol. 11, no. 2, pp. 130–141, 2000.
[2] T. F. Chan, S. Esedoglu, and M. Nikolova, "Algorithms for finding global minimizers of image segmentation and denoising models," *SIAM J. Appl. Math.*, vol. 66, no. 5, pp. 1632–1648, 2006.
[3] D. Cremers, M. Rousson, and R. Deriche, "A review of statistical approaches to level set segmentation: integrating color, texture, motion and shape," *Int. J. Comput. Vis.*, vol. 72, no. 2, pp. 195–215, 2007.
[4] Y. Boykov and G. Funka-Lea, "Graph cuts and efficient N-D image segmentation," *Int. J. Comput. Vis.*, vol. 70, pp. 109—-131, 2006.
[5] C. Couprie, L. Grady, L. Najman, and H. Talbot, "Power watershed: A unifying graph-based optimization framework," *IEEE Trans. Pattern Anal. Mach. Intell.*, vol. 33, no. 7, pp. 1384–1399, 2011.
[6] T. Schoenemann, F. Kahl, S. Masnou, and D. Cremers, "A linear framework for region-based image segmentation and inpainting involving curvature penalization," *Int. J. Comput. Vis.*, vol. 99, no. 1, pp. 53–68, 2012.
[7] N. Y. El-Zehiry and L. Grady, "Contrast driven elastica for image segmentation," *IEEE Trans. Image Process.*, vol. 25, no. 6, pp. 2508–2518, 2016.
[8] W. Zhu, X.-C. Tai, and T. Chan, "Image segmentation using euler's elastica as the regularization," *J. Sci. Comput.*, vol. 57, no. 2, pp. 414–438, 2013.
[9] R. Prevost, R. Cuingnet, B. Mory, L. D. Cohen, and R. Ardon, "Tagged template deformation," in *Proc. MICCAI*. Springer, 2014, pp. 674–681.
[10] X. Bresson, P. Vandergheynst, and J.-P. Thiran, "A variational model for object segmentation using boundary information and shape prior driven by the Mumford-Shah functional," *Int. J. Comput. Vis.*, vol. 68, no. 2, pp. 145–162, 2006.
[11] T. Chan and W. Zhu, "Level set based shape prior segmentation," in *Proc. CVPR*, vol. 2. IEEE, 2005, pp. 1164–1170.
[12] D. Cremers, F. R. Schmidt, and F. Barthel, "Shape priors in variational image segmentation: Convexity, lipschitz continuity and globally optimal solutions," in *Proc. CVPR*. IEEE, 2008, pp. 1–6.
[13] D. Chen, J.-M. Mirebeau, and L. D. Cohen, "Finsler geodesics evolution model for region based active contours," in *Proc. BMVC*, 2016.
[14] ——, "Global minimum for a Finsler elastica minimal path approach," *Int. J. Comput. Vis.*, vol. 122, no. 3, pp. 458–483, 2017.
[15] L. Gorelick, O. Veksler, Y. Boykov, and C. Nieuwenhuis, "Convexity shape prior for binary segmentation," *IEEE Trans. Pattern Anal. Mach. Intell.*, vol. 39, no. 2, pp. 258–271, 2016.
[16] O. Veksler, "Star shape prior for graph-cut image segmentation," in *Proc. ECCV*. Springer, 2008, pp. 454–467.
[17] V. Gulshan, C. Rother, A. Criminisi, A. Blake, and A. Zisserman, "Geodesic star convexity for interactive image segmentation," in *Proc. CVPR*. IEEE, 2010, pp. 3129–3136.
[18] L. A. Royer, D. L. Richmond, C. Rother, B. Andres, and D. Kainmueller, "Convexity shape constraints for image segmentation," in *Proc. CVPR*, 2016, pp. 402–410.
[19] L. Gorelick and O. Veksler, "Multi-object convexity shape prior for segmentation," in *Proc. EMMCVPR*. Springer, 2017, pp. 455–468.
[20] H. Isack, O. Veksler, M. Sonka, and Y. Boykov, "Hedgehog shape priors for multi-object segmentation," in *Proc. CVPR*, 2016, pp. 2434–2442.
[21] H. Isack, L. Gorelick, K. Ng, O. Veksler, and Y. Boykov, "K-convexity shape priors for segmentation," in *Proc. ECCV*, 2018, pp. 36–51.
[22] S. Luo, X.-C. Tai, L. Huo, Y. Wang, and R. Glowinski, "Convex shape prior for multi-object segmentation using a single level set function," in *Proc. CVPR*, 2019, pp. 613–621.
[23] X. Shi and C. Li, "Convexity preserving level set for left ventricle segmentation," *Magn. Reson. Imaging*, vol. 78, pp. 109–118, 2021.
[24] S. Yan, X.-C. Tai, J. Liu, and H.-Y. Huang, "Convexity shape prior for level set-based image segmentation method," *IEEE Trans. Image Process.*, vol. 29, pp. 7141–7152, 2020.
[25] E. Bae, X.-C. Tai, and Z. Wei, "Augmented lagrangian method for an euler's elastica based segmentation model that promotes convex contours," *Inverse. Probl. Imaging*, vol. 11, no. 1, pp. 1–23, 2017.
[26] M. Kass, A. Witkin, and D. Terzopoulos, "Snakes: Active contour models," *Int. J. Comput. Vis.*, vol. 1, no. 4, pp. 321–331, 1988.
[27] L. D. Cohen and R. Kimmel, "Global minimum for active contour models: A minimal path approach," *Int. J. Comput. Vis.*, vol. 24, no. 1, pp. 57–78, 1997.
[28] J. Melonakos, E. Pichon, S. Angenent, and A. Tannenbaum, "Finsler active contours," *IEEE Trans. Pattern Anal. Mach. Intell.*, vol. 30, no. 3, pp. 412–423, 2008.
[29] G. Peyré, M. Péchaud, R. Keriven, and L. D. Cohen, "Geodesic methods in computer vision and graphics," *Foundations and Trends® in Computer Graphics and Vision*, vol. 5, no. 3–4, pp. 197–397, 2010.
[30] R. Duits, S. P. Meesters, J.-M. Mirebeau, and J. M. Portegies, "Optimal paths for variants of the 2D and 3D Reeds–Shepp car with applications in image analysis," *J. Math. Imag. Vis.*, vol. 60, no. 6, pp. 816–848, 2018.
[31] J.-M. Mirebeau, "Fast-marching methods for curvature penalized shortest paths," *J. Math. Imag. Vis.*, vol. 60, no. 6, pp. 784–815, 2018.
[32] J.-M. Mirebeau and J. Portegies, "Hamiltonian fast marching: a numerical solver for anisotropic and non-holonomic eikonal PDEs," *Image Processing On Line*, vol. 9, pp. 47–93, 2019.
[33] B. Appleton and H. Talbot, "Globally optimal geodesic active contours," *J. Math. Imaging Vis.*, vol. 23, no. 1, pp. 67–86, 2005.
[34] V. Appia and A. Yezzi, "Active geodesics: Region-based active contour segmentation with a global edge-based constraint," in *Proc. ICCV*. IEEE, 2011, pp. 1975–1980.
[35] J. Mille, S. Bougleux, and L. D. Cohen, "Combination of piecewise-geodesic paths for interactive segmentation," *Int. J. Comput. Vis.*, vol. 112, no. 1, pp. 1–22, 2015.
[36] D. Chen, J. Zhu, X. Zhang, M. Shu, and L. D. Cohen, "Geodesic paths for image segmentation with implicit region-based homogeneity enhancement," *IEEE Trans. Image Process.*, vol. 30, pp. 5138–5153, 2021.
[37] A. Chambolle and T. Pock, "Total roto-translational variation," *Numer. Math.*, vol. 142, no. 3, pp. 611–666, 2019.
[38] J. A. Sethian and A. Vladimirsky, "Ordered upwind methods for static Hamilton–Jacobi equations: Theory and algorithms," *SIAM J. Numer. Anal.*, vol. 41, no. 1, pp. 325–363, 2003.
[39] J.-M. Mirebeau, "Riemannian fast-marching on Cartesian grids, using Voronoi's first reduction of quadratic forms," *SIAM J. Numer. Anal.*, vol. 57, no. 6, pp. 2608–2655, 2019.
[40] J. A. Sethian, "Fast marching methods," *SIAM Review*, vol. 41, no. 2, pp. 199–235, 1999.
[41] W.-K. Jeong and R. T. Whitaker, "A fast iterative method for eikonal equations," *SIAM J. Sci. Comput.*, vol. 30, no. 5, pp. 2512–2534, Jul. 2008.
[42] T. Deschamps and L. D. Cohen, "Fast extraction of minimal paths in 3D images and applications to virtual endoscopy," *Med. Image Anal.*, vol. 5, no. 4, pp. 281–299, 2001.
[43] S. Zhu and A. Yuille, "Region competition: Unifying snakes, region growing, and Bayes/MDL for multiband image segmentation," *IEEE Trans. Pattern Anal. Mach. Intell.*, vol. 18, no. 9, pp. 884–900, 1996.
[44] T. F. Chan and L. A. Vese, "Active contours without edges," *IEEE Trans. Image Process.*, vol. 10, no. 2, pp. 266–277, 2001.
[45] D. Chen, J.-M. Mirebeau, H. Shu, and L. D. Cohen, "Eikonal region-based active contours for image segmentation," *arXiv preprint arXiv:1912.10122*, 2019.
[46] S. Alpert, M. Galun, A. Brandt, and R. Basri, "Image segmentation by probabilistic bottom-up aggregation and cue integration," *IEEE Trans. Pattern Anal. Mach. Intell.*, vol. 34, no. 2, pp. 315–327, 2012.
[47] J.-M. Mirebeau, L. Gayraud, R. Barrère, D. Chen, and F. Desquilbet, "Massively parallel computation of globally optimal shortest paths with curvature penalization," *Pre-Print*, 2021.

Da Chen received his Ph.D degree in applied mathematics from CEREMADE, University Paris Dauphine, PSL Research University, Paris, France, in 2017. From 2017 to 2019, he worked as a post-doctoral researcher at CEREMADE, University Paris Dauphine, and also at Centre Hospitalier National d'Ophtalmologie des Quinze-Vingts, Paris, France. Now he is working in Shandong Artificial Intelligence Institute,

Qilu University of Technology (Shandong Academy of Sciences). His research interests include variational methods, partial differential equations, and geometric methods as well as their applications in computer vision and image analysis, such as minimal geodesic paths, active contours, image/volume segmentation, tubular structure tracking, surface reconstruction and medical image registration.

Jean-Marie Mirebeau is a director of research in applied mathematics from the French CNRS (National Center for Scientific Research), working in Centre Borelli of the Ecole Normale Superieure of Paris-Saclay, University Paris-Saclay. His main subject of research is the numerical analysis of PDEs, focusing on difficulties related to strong anisotropies, which are addressed using tools from discrete geometry. He also studies PDE-based image analysis, and distributes open source numerical codes of his work. He defended his Ph.D. at University Pierre et Marie Curie in 2010, prepared under the supervision of Prof. Albert Cohen, and is a former student of the Ecole Normale Supérieure of Paris. Jean-Marie Mirebeau received in 2016 the 9th Popov prize, which is an international prize awarded every three years for contributions in approximation theory.

Minglei Shu received his B.S. degree in automation from Shandong University in 2003, the M. Sc. degree in power electronics and power transmission from Shandong University in 2006 and Ph.D. degree in communication and information systems from Shandong University in 2016. Currently, he is working at Shandong Artificial Intelligence Institute, Qilu University of Technology (Shandong Academy of Sciences), and Deputy Director of Shandong Artificial Intelligence Institute. His research interests mainly include computer vision, medical image segmentation, 3D blood vessel segmentation and tracking, IoT medical care as well as wireless sensor networks.

Xuecheng Tai is currently a member of the Department of Mathematics, Hong Kong Baptist University. His research interests include numerical partial differential equations, optimization techniques, inverse problems, and image processing. He has done significant research work in his research areas and published in top quality international conference and journals. He is the winner of the eight Feng Kang Prize for scientific computing. He has served as organizing and program committee member for many international conferences and has been often invited for international conferences. He has served as editors, referees, and reviewers for many premier conferences and journals.

Laurent D. Cohen was student at the Ecole Normale Superieure, rue d'Ulm in Paris, France, from 1981 to 1985. He received the Master's and Ph.D. degrees in applied mathematics from University of Paris 6, France, in 1983 and 1986, respectively. He got the Habilitation á diriger des Recherches from University Paris 9 Dauphine in 1995. From 1985 to 1987, he was member at the computer graphics and image processing group at Schlumberger Palo Alto Research, Palo Alto, California, and Schlumberger Montrouge Research, Montrouge, France, and remained consultant with Schlumberger afterward. He began working with INRIA, France, in 1988, mainly with the medical image understanding group EPIDAURE. He obtained in 1990 a position of Research Scholar (Charge then Directeur de Recherche 1st class) with the French National Center for Scientific Research (CNRS) in the Applied Mathematics and Image Processing group at CEREMADE, Universite Paris Dauphine, Paris, France. His research interests and teaching at university are applications of partial differential equations and variational methods to image processing and computer vision, such as deformable models, minimal paths, geodesic curves, surface reconstruction, image segmentation, registration and restoration. He is currently or has been editorial member of the Journal of Mathematical Imaging and Vision, Medical Image Analysis and Machine Vision and Applications. He was also member of the program committee for about 50 international conferences. He has authored about 260 publications in international Journals and conferences or book chapters, and has 6 patents. In 2002, he got the CS 2002 prize for Signal and Image Processing. In 2006, he got the Taylor & Francis Prize: "2006 prize for Outstanding innovation in computer methods in biomechanics and biomedical engineering." He was 2009 laureate of Grand Prix EADS de l'Academie des Sciences in France. He was promoted as IEEE Fellow 2010 for contributions to computer vision technology for medical imaging.